Int J Fract (2026) 250:11
https://doi.org/10.1007/s10704-025-00902-x

RESEARCH

A novel model for corrosion-induced cracking and spalling in reinforced concrete structures

II-FE models of beams: an analysis of bond-slip degradation, corroded steel, spalling of the concrete cover, and stirrup confinement

J. Alfaiate · L. J. Sluys · A. Costa

Received: 22 August 2025 / Revised: 19 November 2025 / Accepted: 17 December 2025

Abstract In the present work, macro-mechanical modelling of reinforced concrete structures under corrosion is performed. A traction based damage model is adopted. A discrete crack approach is used to model the fracture behaviour of concrete. The bond-slip relation between reinforcement steel and concrete is continuously evolving under corrosion, as a function of corrosion level and stress state. This is a non trivial issue, which is dealt with taking into account a total approach. Other corrosion aspects considered in this work are the reduction of the sane cross section of the reinforcement steel as well as spalling of the concrete cover. Bending tests are performed to evaluate the influence of corrosion at structural level, namely the increase of deformation as well as the decrease of the strength of the structure, leading to premature failure. Furthermore, stirrup confinement, in association with spalling, and slippage of the anchorage zone are analyzed.

Keywords Corrosion · Reinforced Concrete · Spalling of concrete cover

J. Alfaiate (✉) · A. Costa
Instituto Superior Têcnico, Universidade de Lisboa Av. Rovisco Pais 1, Lisboa, Portugal
e-mail: jorge.alfaiate@tecnico.ulisboa.pt

L. J. Sluys
Delft University of Technology, P.O. Box 5048, 2600 GA Delft, The Netherlands

List of symbols

DSDA	Discrete Strong Discontinuity Approach
IA	Incremental Approach
TIA	Total Iterative Approach
$\|.\|$	the norm of (.)
C	control loading function used with the Total Iterative Approach
c_0	initial cohesion
c	cohesion
d	scalar damage variable
$\mathbf{d}$	second order damage tensor
d_n	normal damage variable component
d_s	shear damage variable component
D_{nn}	normal diagonal component of tensor $\mathbf{D}^{el}_{\Gamma_d}$
D_{ss}	shear diagonal component of tensor $\mathbf{D}^{el}_{\Gamma_d}$
$\mathbf{D}^{el}_{\Gamma_d}$	second order elastic constitutive tensor
Δ	increment
f_1, f_2	limit surfaces defined in the traction space
f_{t0}	initial tensile strength
f_t	tensile strength
$\mathbf{F}$	Applied force vector
G_F	fracture energy
G_F^{II}	fracture energy under mode-II fracture
g_n	normal damage evolution law
g_s	shear damage evolution law
κ	monotonic increasing function of the displacement jump components
λ	loading factor
ρ	κ_s/κ_n

$\boldsymbol{\sigma}$	stress tensor
$\boldsymbol{\varepsilon}$	strain tensor
$\mathbf{t}$	traction vector acting at the discontinuity
t_n	normal component of the traction vector
t_s	shear component of the traction vector
$\mathbf{w}$	displacement jump vector
w_n	normal component of the jump displacement vector
w_s	shear component of the jump displacement vector
ϕ	internal friction angle; diameter of reinforcement bar

1 Introduction

Corrosion of the reinforcement steel is the main durability issue in reinforced concrete structures. The mechanism of steel corrosion is based on chemo-hygro-thermo-mechanical processes (Ožbolt et al. 2017). Some important mechanical effects due to corrosion are (Fang et al. 2004, 2006; Guzmán et al. 2011, 2012, 2014; Guzmán and Gálvez 2017; Sanz et al. 2013, 2015, 2016, 2017; P.Broomfield 1997; Jiang et al. 2018; Lin et al. 2014):

(i) degradation of steel to concrete bond,
(ii) reduction of the resistant cross section area of the steel bars, also designated by core reduction hereafter,
(iii) expansion of the steel cross section due to the formation of rust around the steel bars, which may cause delamination and spalling of the cover.

All these mechanisms induce damage in the structure, leading to an increase of cracking and deformation, as well as a decrease of strength. In part I of this work, strategies are proposed to deal with these issues. In Section 2, a concise summary of the main aspects of the model and the iterative approach is presented.

In Section 3, numerical bending tests are presented. Different from the work presented in Alfaiate et al. (2023), the main reinforcement is modelled with isoparametric elements, allowing to enforce the expansion of the corroded steel.

The purpose of the numerical tests is twofold:

(a) quantifying the effect of the corrosion on the ultimate limit state;
(b) evaluating the effect of the corrosion under serviceability conditions.

In the former case, the ultimate load is obtained in each test and compared to the non-corroded ultimate load. In the latter case, the results are analyzed at both structural level and local level. At structural level the load-displacement response, stiffness degradation and cracking are analyzed. At local level stress analysis, bond-slip behaviour and crack evolution are investigated.

In Section 3.1, the effects of the degradation of the bond-slip due to corrosion are considered. In Section 3.2, the effect of the reduction of the cross section of the bar is analyzed. In Section 3.3, the dependence on mixed-mode and mode-II under compression is analyzed. In Section 3.4, concrete spalling is studied. In Section 3.5, stirrup confinement is analyzed. In Section 3.6, corrosion is introduced only at the central zone of the beam and in Section 3.7, the effect of premature failure due to slippage of the anchorage is presented. Finally, in Section 4, experimental validation of the model is performed.

2 Material and numerical model

The material and numerical model is detailed in part I of this work. A new damage model is introduced for cohesive fracture, in which the damage evolution law is driven by the traction field. For this purpose, a limit surface in the traction space is defined (see Fig.1 in part I). The model is based upon the following definitions:

A. Fracture mode
B. Traction state on the limit surface
C. Energy dissipation
D. Damage driving mechanism
E. Return mapping.

The concept of *damage driving mechanism* is an important novel aspect of the model, allowing to take into account both mixed-mode fracture and corrosion.

Three main aspects are considered due to the direct influence of corrosion: reduction of the sane cross section of the reinforcement bar, deterioration of the bond-slip relation between steel and concrete and spalling due to volume expansion of the main reinforcement. Degradation of steel to concrete bond is defined as the transition between bond-slip relationships, obtained experimentally, evolving with corrosion level.

An iterative procedure is adopted, based on a total approach, using a return mapping algorithm to track traction evolution.

Items A. to E. are summarized in appendix A, Table 2. In Table 3, the possible combinations among fracture mode, traction on the limit surface, damage driving mechanism and return mapping are listed.

3 Numerical tests

In the following, numerical bending tests on reinforced concrete subjected to corrosion are presented. The finite element mesh and boundary conditions are presented in Fig.1. The beam is simply supported and is 2 meters long ($L = 2000$ mm), 0.20 m high ($h = 200$ mm) and 0.30 m thick ($b = 300$ mm). The load (pre-corrosion p_1 and post-corrosion p_2) is uniformly distributed on all top nodes of the beam. The properties adopted for concrete are:

Young's modulus	character. strength	tensile strength	fracture energy
$E_c = 32$ GPa	$f_{ck} = 27.4$ MPa	$f_t = 3$ MPa	$G_F = 0.1$ N/mm

The bulk behaviour of concrete is elastic under tensile stresses, whereas concrete compressive behaviour is modelled as elastic-perfectly plastic. A discrete crack approach is adopted with bilinear softening for mode-I cracking.

The beam is reinforced with 3 bars of 16 mm ($3\phi16$) of steel S400:

Young's modulus	characteristic strength	design strength
$E_s = 200$ GPa	$f_{yk} = 400$ MPa	$f_{yd} = 348$ MPa

An elastic-perfectly plastic model is adopted for the steel behaviour. The centre of gravity of the steel bar is 40 mm from the bottom of the beam, i.e., the cover is equal to 320 mm and the effective height is $d = 200 - 40 = 160$ mm.

In the tests without corrosion performed in the following, an ultimate load of $p_u \approx 70$ kN/m is estimated (see appendix C, Eq. (11)).

The pre-corrosion and post-corrosion bond-slip laws are given in Figure 2 and in Table 5 of appendix D. The latter corresponds to a corrosion level η_f of 20%. The level of corrosion η is defined according to:

$$\eta = \frac{A_0 - A}{A_0}, \tag{1}$$

where A_0 is the initial cross sectional area of the bar and A is the uncorroded cross sectional area of the bar, after removing the corrosion sub-products. These curves are taken from the works presented in Silva (2018); Wu and Zhao (2013); Jiang et al. (2018), where values of $\eta \in [3\% - 20\%]$ are considered. The value of $\eta = 20\%$ is considered in this work in order to emphasize the effect of the material deterioration in the structural behaviour of the beams.

At the steel-concrete interface a normal elastic stiffness equal to $D_{nn} = 10^5$ N/mm is adopted, which is large enough to prevent overlapping between both materials. The shear elastic stiffness is obtained from the experimental results according to Table 5, leading to $D_{ss} = 6.371/0.20 = 31.855$ N/mm. In order to simulate the effect of the anchorage length, the steel-concrete connection at the top left edge of the bar is very stiff ($D_{nn} = D_{ss} = 10^9$ N/mm), (see Fig.1).

Only half of the beam is modelled due to symmetry. The concrete bulk is modelled using 4 node isoparametric elements. Several vertical prescribed cracks are defined across the length of the specimen in order to model multiple cracking due to tension-stiffening. These cracks are modelled using zero thickness linear interface elements

1st crack	2nd crack	3rd crack	4th crack	5th crack
500 mm	640 mm	800 mm	900 mm	1000 mm (midspan)

Location of prescribed discontinuities along half the length of the beam (mm)

In the work presented in Alfaiate et al. (2023), the reinforcement bar is modelled using truss elements. Here, the steel bar is modelled adopting 4 node isoparametric elements, with zero thickess linear interface elements above and underneath the bar. In this way, it is possible to enforce the volume expansion due to spalling. Moreover, apart from the bond-slip relationship, it is also possible to properly take into account the normal traction between concrete and steel. A correct measurement of both normal and shear tractions at the

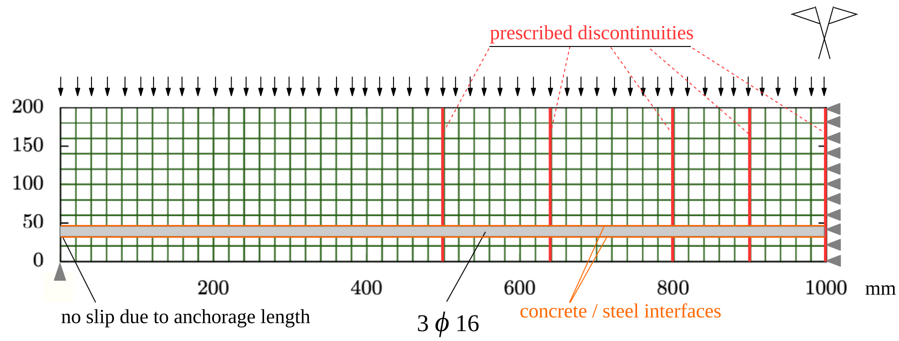

Fig. 1 Reinforced concrete beam: boundary conditions and adopted mesh

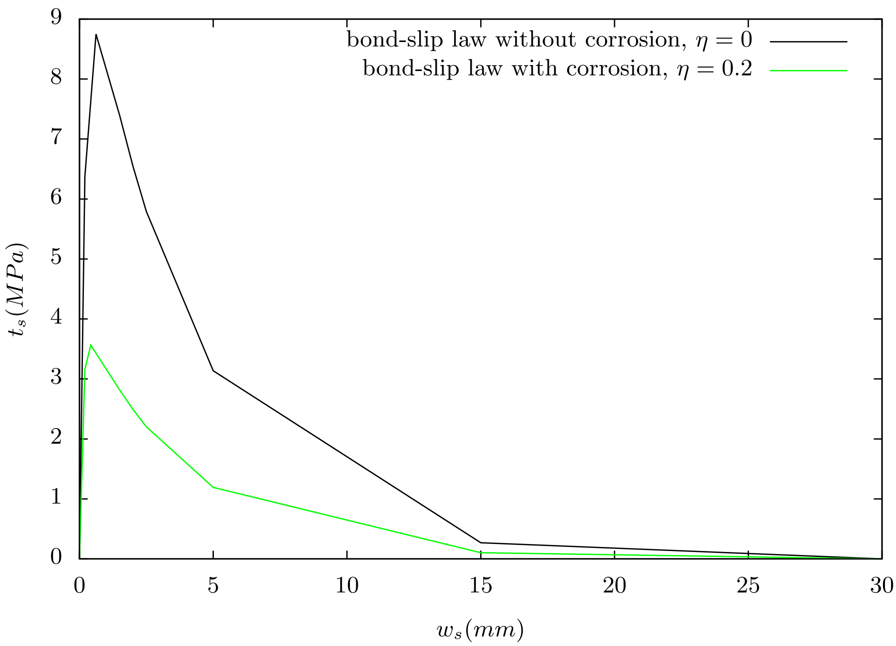

Fig. 2 Bond-slip laws adopted without and with corrosion

interfaces is essential to consider mixed-mode fracture as well as bond behaviour under compression.

In light of this new mesh discretization as well as the new material and numerical model, the influence of the following phenomena is studied:

(i) the degradation of the bond-slip law due to corrosion;
(ii) the reduction of the effective cross section of the reinforcement bar;
(iii) the dependence of the bond-slip law on the the normal traction at the interface under both mode-II fracture under compression and mixed-mode fracture;
(iv) concrete spalling;
(v) stirrup confinement;
(vi) slippage at the anchorage zone.

These effects are treated separately, but are stepwise introduced in an integrated model; for instance, the reduction of the cross section of the bar (ii) will always be taken into account after it is introduced in Section 3.2.

In the tests performed, the criteria adopted for crack evolution, steel concrete interface and corrosion, are summarized in Appendix B.

During the corrosion stage, bond-slip evolution is defined under constant load, according to the transition mode introduced in part I. Afterwards, a mode-II damage driving mechanism is adopted at the corroded steel-concrete interfaces (line 6 in Table 3). In Section 3.3, both radial return mapping and no prescribed return mapping are adopted (lines 9 and 12 in Table 3), with both linear and quadratic modified fracture energy laws (items e1. and e2., respectively, in Tables 2 and 3).

3.1 Degradation of the bond-slip law due to corrosion

In the first test, designated hereafter as reference test, the beam is not subjected to corrosion. The solution is obtained under displacement control: in each step, a displacement increment at midspan $\Delta u_k^* = -0.02$ mm (↓) is enforced. In Fig.3, the deformed mesh obtained for maximum deformation is shown[1]. In this Figure, it is clear that crack opening occurs at all vertical prescribed discontinuities. The maximum load obtained from the test is $p_u = 76$ kN/m, corresponding to a vertical nodal force of 750 N (see Fig.4).

The tensile strength of concrete ($f_t = 3$ MPa) is first reached at the central fictitious crack, at the symmetry line[2]. Each load drop in the reference load-displacement curve corresponds to crack opening at another prescribed discontinuity due to tension-stiffening, which occurs simultaneously with unloading of the other fictitious cracks.

Next, the test with corrosion is performed under non-proportional loading, with the following three loading stages:

i. the load is applied (using 1.(a), 2.(a) in Table 4), until a value of the force p_1 is reached, where p_1 is the pre-corrosion distributed load. The corrosion is introduced at three different load levels, defined by the vertical nodal force F_1 at midspan)
   1. F_1=153 N, corresponding to displacement $u =$ 0.6 mm at midspan and distributed load p_1 =15.6 kN/m;
   2. F_1=400 N, corresponding to displacement $u =$ 4.0 mm at midspan and distributed load p_1 =40.8 kN/m;
   3. F_1=570 N, corresponding to displacement $u =$ 6.0 mm at midspan and distributed load p_1 =58.2 kN/m.

ii. keeping the load p_1 fixed, corrosion is introduced (case 3.(a) in Table 4), according to the following control function (see part I):

$$C = \lambda_t^j - (\lambda_{t-1} + \frac{\Delta\eta^*}{\eta_f}) = 0, \tag{2}$$

adopting 10 increments of $\Delta\eta^*$, until a value of the final corrosion level $\eta_f = 0.2$ is reached; thus, at this stage all effects due to corrosion are implemented in a stepwise manner, namely the degradation of the bond-slip law, according to Section 4.2 in part I, the reduction of the effective cross section, from Section 3.2 onwards, slippage, from Section 3.4 onwards and the loss of anchorage (Section 3.7);

iii. next, the post-corrosion load p_2 is increased under displacement control (using 1.(a), 2.(a) in Table 4).

In the latter stage, the bond-slip relationship corresponding to the total corrosion level $\eta_f = 20\%$ is adopted.

In Fig.4, both load-displacement curves obtained with and without corrosion corresponding to loading case 1 (F_1 =153 N) are shown. During the corrosion stage, a small displacement increase at midspan is found (blue curve in the zoom window). In stage iii., the influence of corrosion is clear. The ultimate load obtained from both tests lies on a *plateau*, in which the steel reinforcement reaches the yield stress, at midspan.

In Figs.5 and 6, the load-displacement curves obtained with corrosion corresponding to loading cases 2 (F_1 =400 N) and 3 (F_1 =570 N), respectively, are also plotted.

In all cases, the most important effect of the corrosion due to the degradation of the bond-slip law is the stiffness decrease, not affecting much the maximum load capacity of the structure.

In Figs.5 and 6, the corrosion stage (item ii.) gives rise to a clear plateau in the load-displacement curves, whereas in the former case (Fig.4) this plateau is only visible in the amplification window shown in the same figure. This is due to the fact that, in the former case (F_1 =153 N), the structural pre-corrosion damage level is much smaller than the structural pre-corrosion damage level obtained in the other cases (F_1 =400 N and F_1 =570 N). Thus, it is observed that degradation of the bond-slip relationship gives rise to a larger increase of damage in severely loaded structures. This conclusion, is emphasized in the following Sections.

[1] A displacement amplification factor of 10 is adopted for all shown deformed meshes, except Figure 18.

[2] definition of fictitious crack is given in Hillerborg et al. (1976), and refers to the pre-crack stage, in which dissipation of energy occurs.

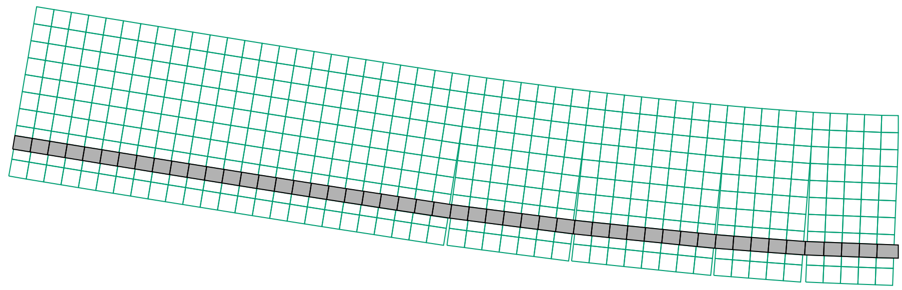

Fig. 3 Reinforced concrete test: deformed mesh (amplification displacement factor = 10)

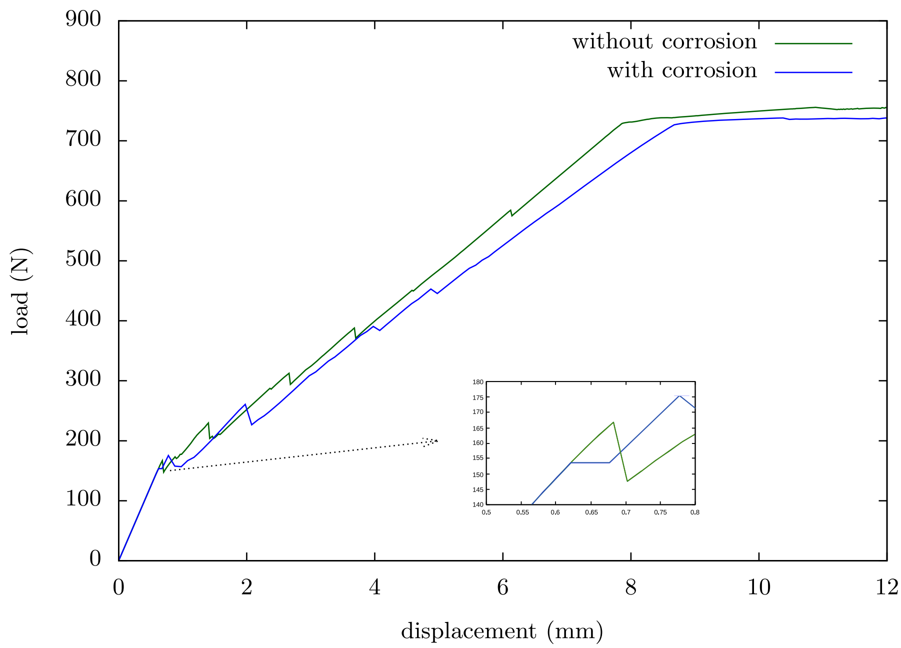

Fig. 4 Load-displacement curves obtained without and with corrosion; case 1, corrosion introduced at $p_1 = 15.6$ kN/m, F_1=153 N

3.2 Reduction of the efective cross section of the reinforcement bar

In this Section, the reduction of the resistant cross section of the reinforcement bar is taken into account.

In Figs. 7 to 9, the load-displacement curves obtained in Figs. 4 to 6 are compared to the load-displacement curves obtained with both degradation of the bond-slip relation and core reduction of the reinforcement bars.

Comparing the results obtained with bond-slip degradation to the results obtained with both bond-slip degradation and core reduction of the cross section of the bar, it can be concluded that:

i) a strong reduction of the ultimate load is obtained due to the reduction of the sane cross section of the steel bars; under bond-slip degradation only, the maximum load decreases from from $F_1 = 760$ N (test without corrosion) to $F_1 \approx 740$ N (3 %), whereas under both bond-slip degradation and core reduction the maximum load decreases from $F_1 = 760$ N to $F_1 \approx 600$ N (79 %). The latter result is in agreement with Equations (9) to (11) in Appendix C, reducing A_s by 20%;the stiffness of the structure decreases even further due to the introduction of core reduction, when compared to the tests where core reduction is not taken into account. In fact, the plateau found in Figs.8 and 9, corresponding to the damage increase under the corrosion stage, is considerably more pronounced than the plateau found in Figs.5 and 6.

ii) in the third test, by introducing corrosion at the vertical displacement of 6.0 mm (see Fig. 9), the remaining strength available afterwards is limited, with the load increasing from F_1=570 N to only F_1=606 N. In fact, the concrete-steel interface fails locally in this case, under the final cor-

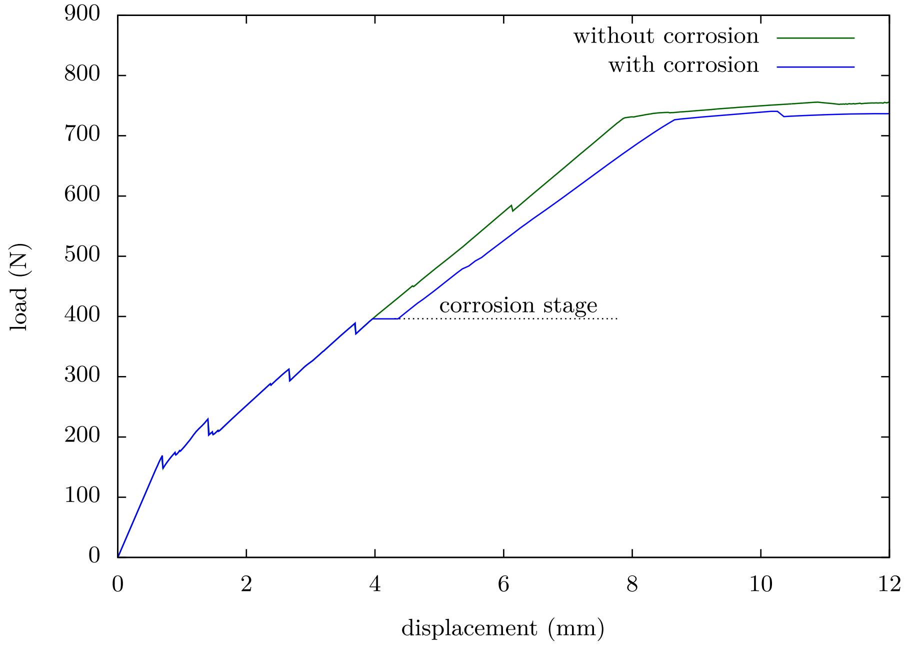

Fig. 5 Load-displacement curves obtained without and with corrosion; case 2, corrosion introduced at $p_1 = 40.8$ kN/m, F_1=400 N

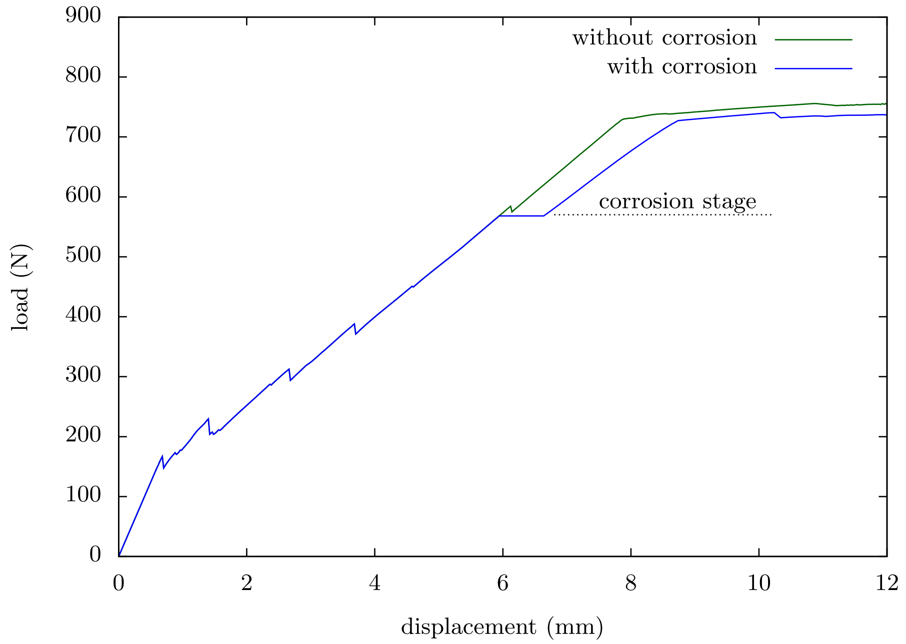

Fig. 6 Load-displacement curves obtained without and with corrosion; case 3, corrosion introduced at $p_1 = 58.2$ kN/mF_1=570 N

rosion level. This happens due to the fact that the shear strength, corresponding to the maximum shear traction capacity available at the interface, decreases to a value below the applied shear traction at $x = 500$ mm. Notwithstanding, if the shear traction is allowed to decrease locally, redistribution of the traction state occurs along the neighbouring interface, and equilibrium can still be re-established. Conversely, this is no longer possible if a larger pre-corrosion displacement is enforced, such as $u = 7$ mm.

Thus, the reduction of the sane cross section of the steel bar has a significant influence on the ultimate load of the structure. In the examples presented in Figs. 4 to 9, the plastic behaviour of the steel is reached when

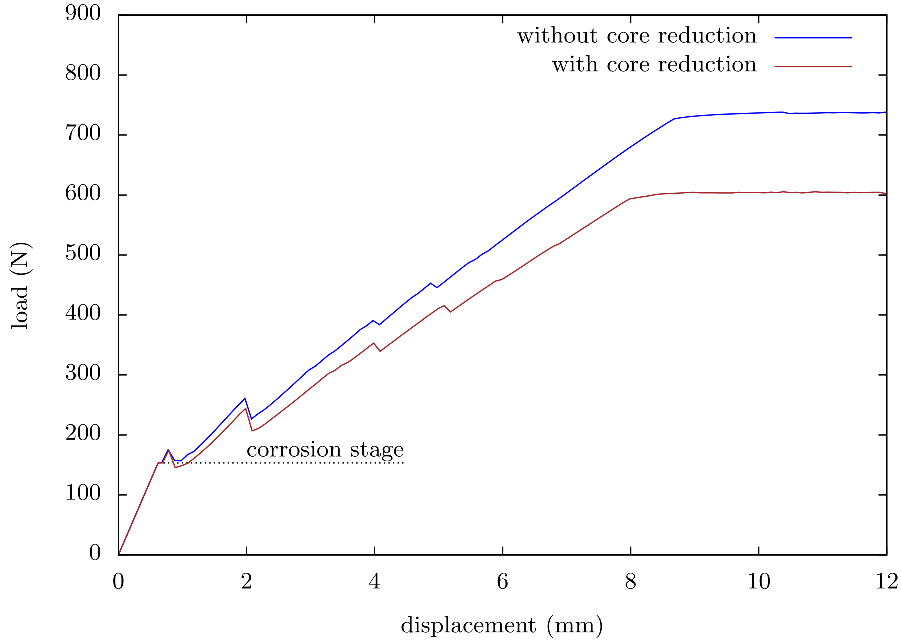

Fig. 7 Load-displacement curves obtained in case 1 (F_1 =153 N), with and without core reduction

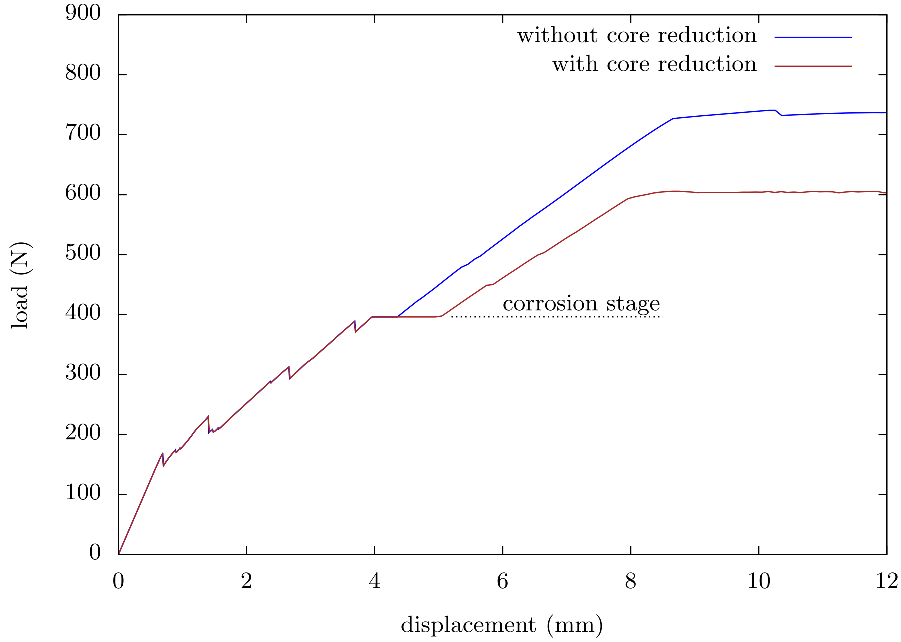

Fig. 8 Load-displacement curves obtained in case 2 (F_1 =400 N), with and without core reduction

the maximum principal stress component σ_I attains the yield stress $f_{yk} = 400$ MPa. In each steel element, the stress used to control the material behaviour is obtained at the centre of the element. This procedure gives rise to results similar to the ones obtained in the work presented in Alfaiate et al. (2023), in which truss elements were adopted for the steel bar.

Nevertheless, the adopted mesh refinement is moderate, such that the stress obtained from the different integration points in the element can differ considerably, in particular near critical points, such as maximum compressive stress at the concrete at the top as well as the maximum tensile stress in the steel, both at midspan. This is why other tests are presented in Figs. 10, 11 to 12, in which the control stress that triggers

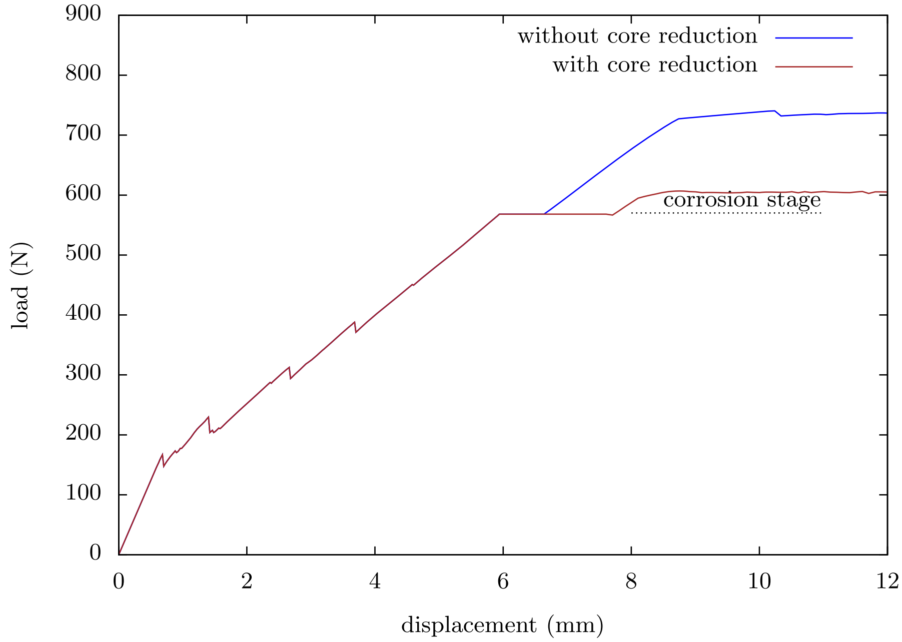

Fig. 9 Load-displacement curves obtained in case 3 (F_1 =570 N), with and without core reduction

nonlinear bulk behaviour, both in the concrete under compression and in the steel, is obtained at the integration point which exhibits the maximum (or minimum) value within each finite element. In these Figures, it is clear that the ultimate load obtained from these tests is reduced by 8%. Moreover, in the third test the load can no longer increase after the corrosion stage, even if redistribution of the traction state occurs along the neighbouring interface is considered, as mentioned above. This is due to the fact that both the steel and the concrete reached the maximum / minimum elastic stress, respectively, and entered the plastic regime before the end of the corrosion stage. In fact, loading case 3 corresponds to the limit case in which the damage under the pre-corrosion stage is too high, such that introducing corrosion will induce failure of the structure.

In the remaining tests, the latter approach is adopted, in which the control stress at the bulk elements is taken from the integration point exhibiting the most critical value. This approach is more conservative, taking into account that the results are very sensitive to the critical stress field obtained near midspan. Moreover, loading case 3 will no longer be considered, due to premature failure under corrosion.

Note that this issue, regarding the evaluation of the stress in the bulk, does not occur in the interface elements. This is due to the fact that these elements are integrated using a Newton-Cotes scheme, such that the tractions are obtained at the nodes, not at the Gauss points. This integration scheme has proved to be more adequate to deal with high stiffness elastic coefficients or penalty functions, as adopted in this work (Kikuchi and Oden 1988; Dias-da-Costa et al. 2007, 2010).

In Fig. 13, the distribution of the maximum principal stress component σ_I obtained in the steel reinforcement along the length of the beam is presented for the three loading cases (F_1 =153, 400, 570 N) as well as for the result obtained without corrosion. It can be observed that crack opening takes place at the three last discontinuities in the case of no corrosion, whereas no opening is obtained in the fourth discontinuity (x = 900 mm) in all examples with corrosion. Thus, corrosion gives rise to a different tension-stiffening process along the beam. An increase of the stress near the support is also observed under corrosion.

3.3 Dependence on the traction normal to the steel-concrete interface

In the work presented in Alfaiate et al. (2023), the steel bar was modelled by means of truss elements, connected by one single line of interface elements to the concrete elements. As a consequence, the bond-slip relationship between the steel bar and the bulk was

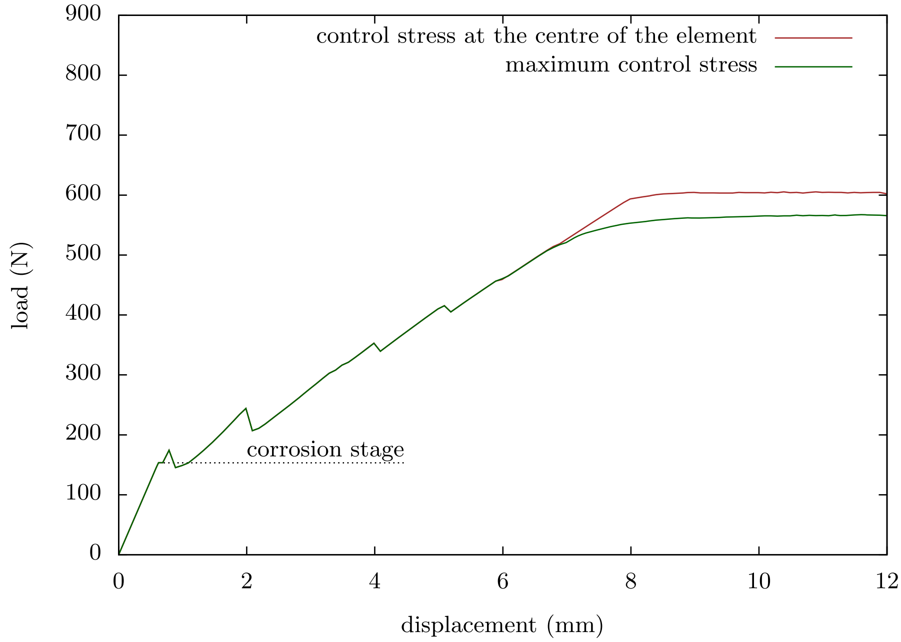

Fig. 10 Load-displacement curves obtained in case 1 (F_1 =153 N), with core reduction

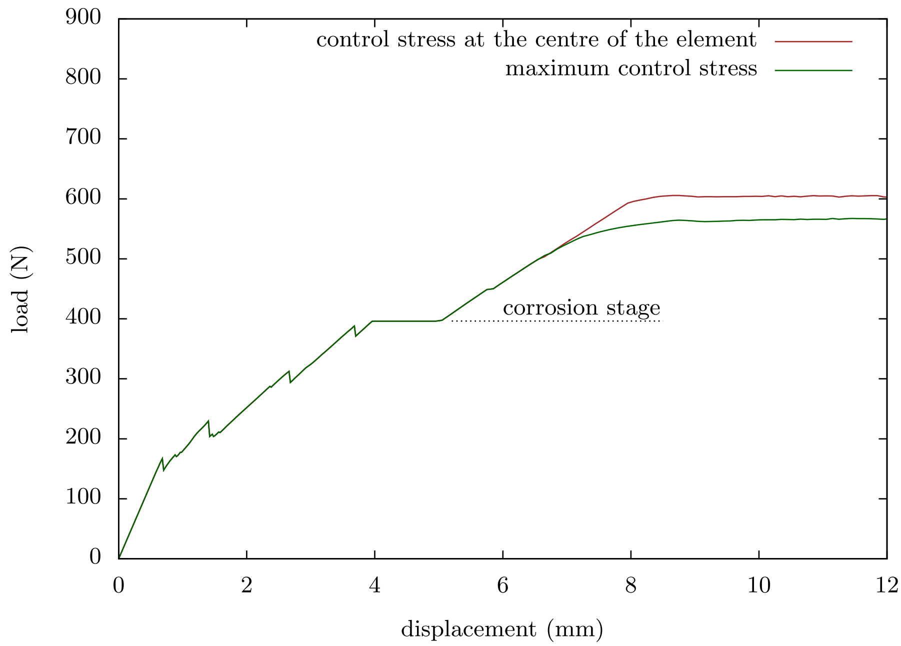

Fig. 11 Load-displacement curves obtained in case 2 (F_1 =400 N), with core reduction

properly approximated. However, the normal traction obtained at the interface did not provide an adequate measure of the action of the bulk material on the reinforcement bars. This is why, instead of the normal traction, the bulk stress value normal to the reinforcement bar, at the neighbourhood of the interface, was considered to measure this action.

In this work, the connection between concrete and steel is modelled by interface elements, located above and below the steel. As such, the corresponding normal traction can now be properly traced.

In the examples from Figs. 7 to 9, no limitation is enforced on the development of the normal traction at the steel-concrete interface (case 2.(a) in Table 4). Although in the work presented in Alfaiate et al. (2023),

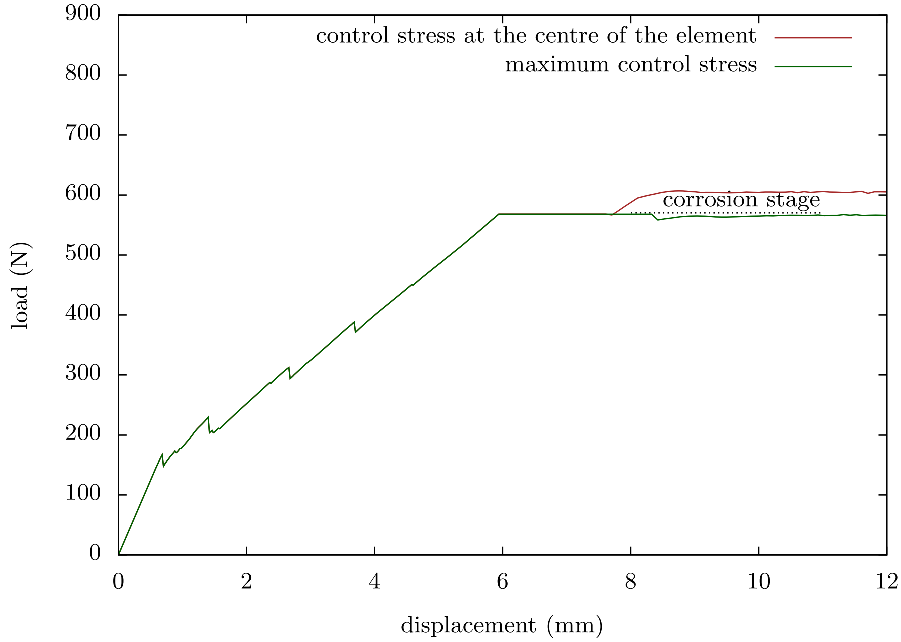

Fig. 12 Load-displacement curves obtained in case 3 (F_1 =570 N), with core reduction

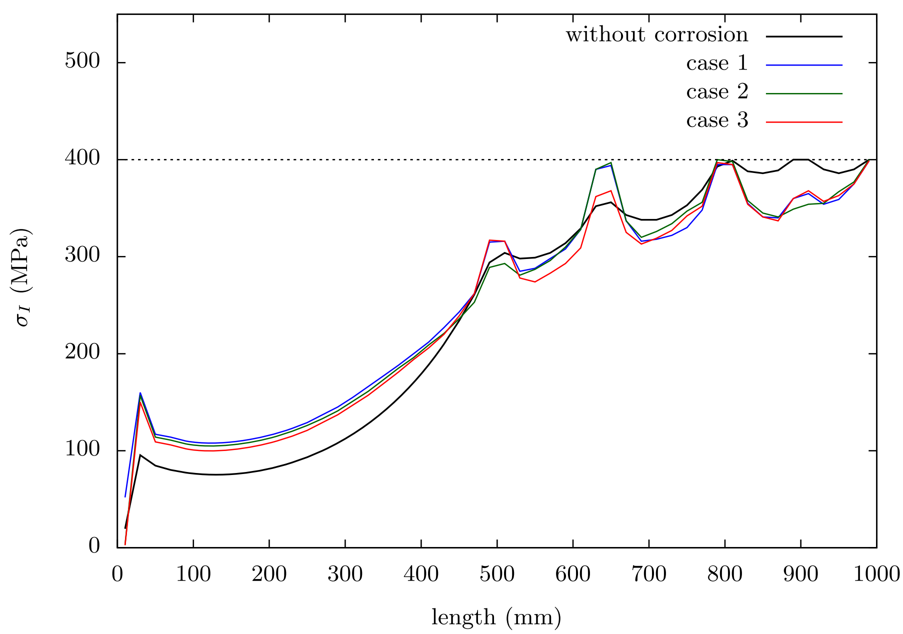

Fig. 13 Distribution of σ_I in the reinforcement steel for the three cases (F_1 =153, 400, 570 N) and for the beam without corrosion

the bulk tensile stresses normal to the interface were found to be relatively small, higher values of the normal traction can be measured at the interface with the current discretization.

In the following, evolution of the bond-slip relation after corrosion is performed under:

i) a mode-II damage driving mechanism with constant normal traction return mapping (case 2.(a) i) in Table 4, line 6 in Table 3);
ii) a mode-II damage driving mechanism with no prescribed return mapping (case 2.(a) ii) in Table 4, line 12 in Table 3).

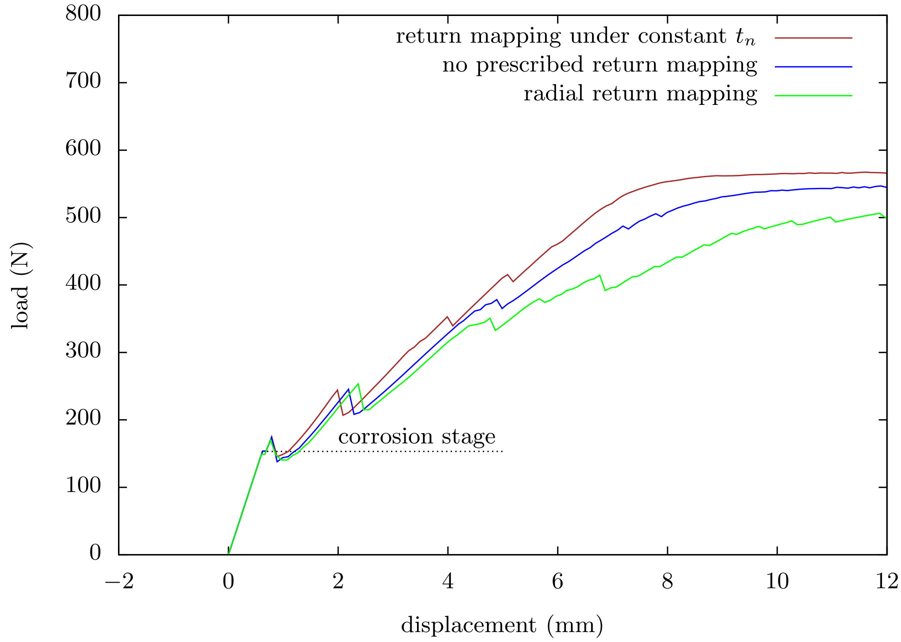

Fig. 14 Load-displacement curves obtained in case 1 (F_1 =153 N), corresponding to items i) to iii)

iii) a generalized mixed-mode driving mechanism with radial return mapping (case 2.(c) ii) in Table 4, line 9 in Table 3).

In cases ii)) and iii)), both the normal and the shear traction are bounded such that the traction state remains either on or below the surface. In case ii)) damage evolution is obtained independently from the normal and the shear law, whereas in case iii)) normal and shear damage evolution depend on each other, according to radial return mapping. In all cases the modification of energy dissipation is either defined by (6), which was also the case in Alfaiate et al. (2023), or by (7).

In Figs. 14 and 15, the comparison between the results obtained with cases i)) to iii)) are presented, for each level of pre-corrosion load.

It is found that the structural response is very sensitive to the tractions at the interface, in particular under mixed-mode fracture. As expected, the most severe damage is obtained with radial return mapping. In cases 2 and 3, both the stiffness and strength are affected.

In Fig.16, the normal traction obtained at the end of the corrosion stage, at the interface below the steel, is presented. In this Figure, the results obtained in loading case 2 (F_1 =400 N), with both unbounded and bounded normal traction are shown. The main differences occur in the neighbourhood of the vertical cracks. The four peaks correspond to cracks 1, 2, 3 and 5. This is due to the fact that, conversely to the example without corrosion (see deformed mesh in Fig. 3), the fourth crack does not fully open below the steel bar. This is clear in Fig.17, where the deformed mesh corresponding to end of the test is shown. In fact, at this final stage, all cracks are stress-free along most of their length, except the fourth crack. The fourth crack reaches the tensile strength very early, immediately after the central crack, under the load $F_1 = 149$ N. However, upon reaching the ultimate load, the fourth crack still did not fully release the normal traction to zero at the bottom. The central crack tends to localize further, at the same time that the deformation decreases in the others. At midspan, the steel bar yields and the steel-concrete interface presents no bond strength, leading to full opening of the central crack.

Note that, in the results obtained with radial return mapping (iii)), the load jumps corresponding to crack opening occur slightly later, when compared to the other results (Figs. 14 and 15). This due to the fact that the bond traction decreases faster in case (iii)). As a consequence, in the tests obtained with (i)), higher bond tractions are transmitted along the steel-concrete interface, leading to a higher degree of tension stiffening which allows for the cracks to open earlier.

If the test continues further, the deformed mesh presented in Fig.18 is obtained. In Fig. 18 no displacement amplification factor is introduced. This advanced stage is obtained under displacement control. All significant

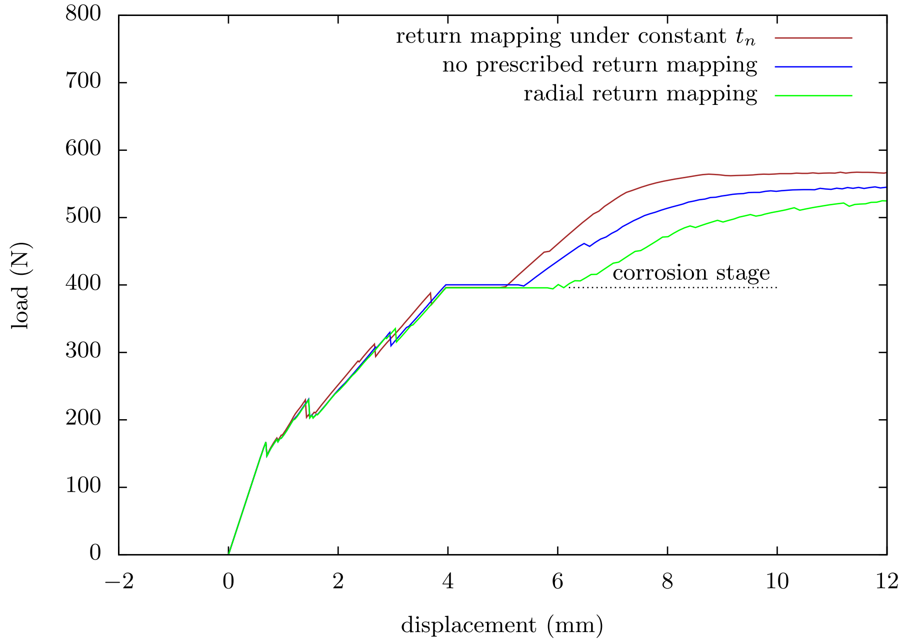

Fig. 15 Load-displacement curves obtained in case 2 (F_1 =400 N), corresponding to items i) to iii)

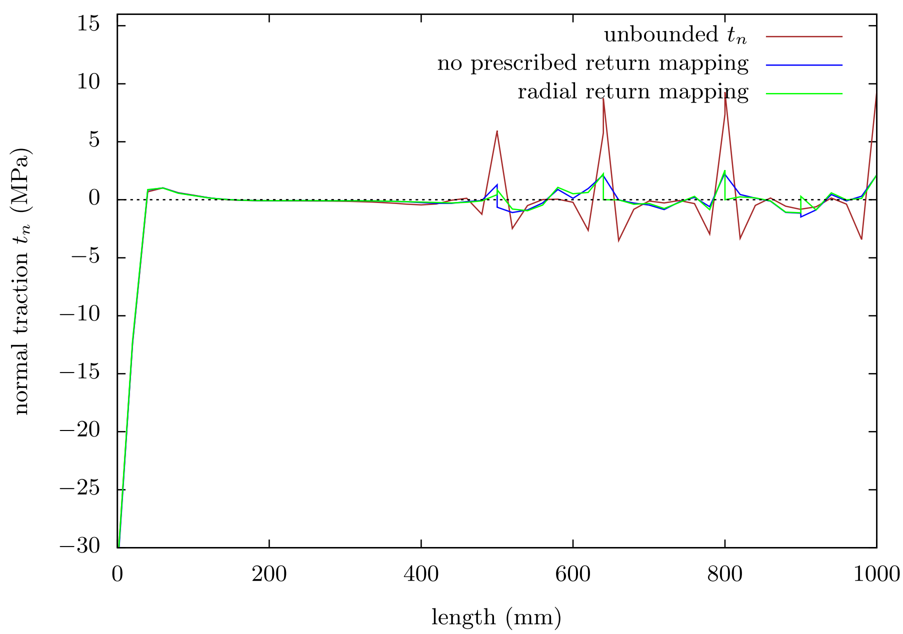

Fig. 16 Distribution of the normal traction along the length of the bar, obtained at the end of the corrosion stage in case 2 (F_1 =400 N)

nonlinear deformation is localized at midspan: opening of the central crack, the steel-concrete bond-slip, concrete crushing and yielding of the steel bar. Along the remaining part of the beam the stress decreases either under softening or due to unloading. Ultimately, the deformed mesh tends to a two rigid body motion, sustained by the steel at midspan.

In Fig. 19, the load-displacement curves obtained under radial return mapping with linear variation of G_F, G_F^{II} (item e1. in Table 2) and quadratic variation of G_F, G_F^{II} (item e2. in Table 2) are presented for loading case 2 (F_1 =400 N). A reduction of both the stiffness and the ultimate load is obtained for the quadratic variation of G_F, G_F^{II}.

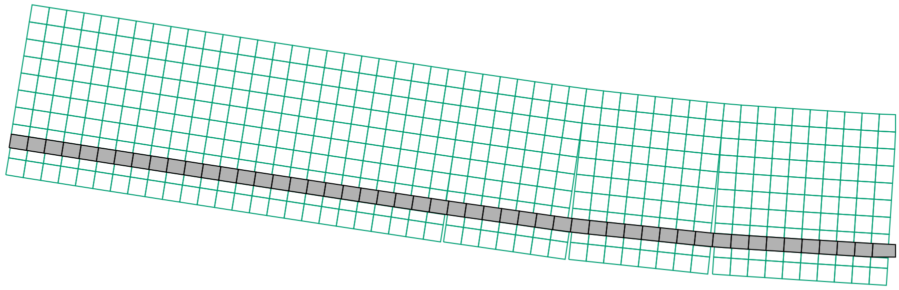

Fig. 17 Deformed mesh obtained under ultimate load with bounded normal traction (F_1 =400 N, amplification displacement factor = 10)

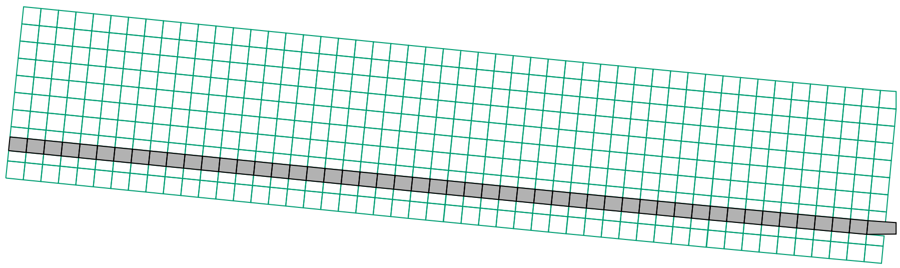

Fig. 18 Deformed mesh obtained at the end of the test with bounded normal traction (F_1 =400 N, no amplification of the displacement)

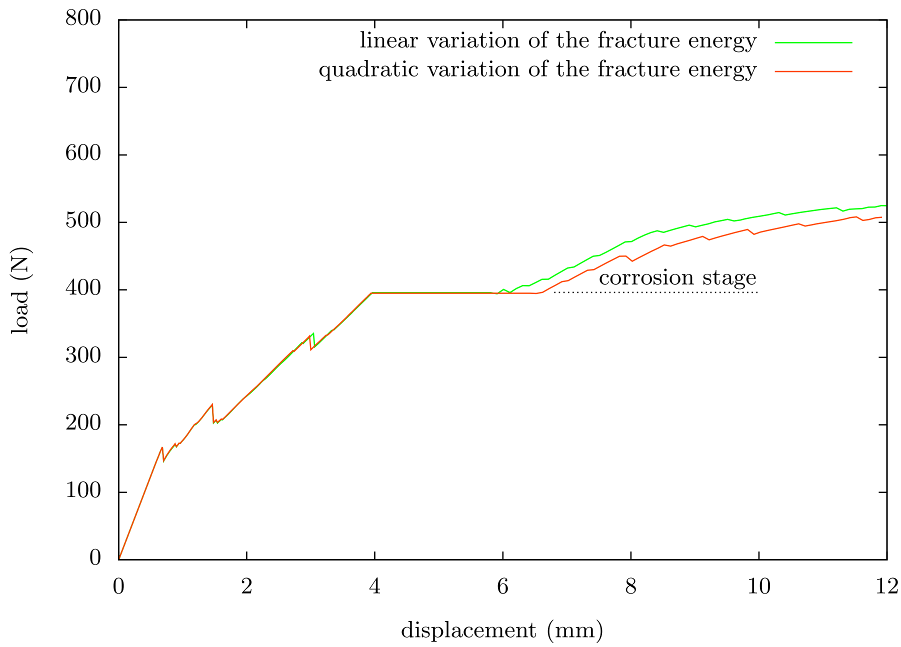

Fig. 19 Load-displacement curves obtained in case 2 (F_1 =400 N), with linear and quadratic variation of fracture energy

Note that the quadratic modification of the fracture energy, when compared to the linear modification of the fracture energy, gives rise to:

i) an increase of energy dissipation, in the case where the material strength increases;
ii) a decrease of energy dissipation, if the material strength decreases.

The former case corresponds to shear under compressive normal traction. Although compressive normal stresses are found along the steel-concrete interface, the elastic bond strength is never reached, and no dissipation of energy is obtained in this case. As a consequence, energy dissipation due to bond-slip only occurs under mixed-mode fracture, corresponding to case ii), as shown in Fig. 19. In the following tests, similar to the work presented in Alfaiate et al. (2023), only a linear variation of the fracture energy is adopted.

3.4 Spalling

In this Section the effect of spalling of concrete is analyzed. Spalling is introduced in two different ways (see part I):

(a) considering volume expansion of the steel reinforcement;
(b) introducing splitting forces at the steel-concrete interface.

In the former case, the volume expansion is obtained by adopting an equivalent temperature increase in the direction perpendicular to the reinforcement length: taking the x direction along the length of the beam, we have

$$\begin{aligned} \varepsilon_{xx}^{\Delta T_{eq}} &= 0, \\ \varepsilon_{yy}^{\Delta T_{eq}} &= \varepsilon_{yy}^{corrosion} = \sqrt{1+\eta} - 1. \end{aligned} \tag{3}$$

In the second case, the expansion of the reinforcement steel is *transferred* to the upper and lower steel-concrete interfaces adjacent to the longitudinal reinforcement. First, no stirrups are considered. In the next Section, both stirrups and compressive steel reinforcement are introduced in the mesh and the corresponding effect is analyzed.

In Figs. 20a and 20b , the load-displacement results obtained neglecting spalling and considering spalling as a volume expansion (a) are presented, for each level of the pre-corrosion load.

In the examples, a translation of the load-displacement results occurs along the x axis (to the left), during the corrosion stage. This is due to the expansion of the cross section of the steel bar, which gives rise to a decrease of the vertical displacement registered at the top of the beam, at midspan. This displacement decrease is found in the two load displacement curves (Figs.20a and 20b), when compared to the solutions without spalling. However, in Fig.20a , since the pre-corrosion displacement is very small, the decrease of the displacement found due to the volume expansion gives rise to a total negative value (upwards), conversely to the case in Fig.20b , in which case the total displacement remains positive (downwards)

In Figs. 21a and 21b , the normal and the shear traction distribution obtained along the bottom steel-concrete interface are presented, at the end of the test corresponding to loading case 1. In Figs. 22a and 22b , the normal and the shear traction obtained along the upper steel-concrete interface are presented, at the end of the test corresponding to loading case 1. The results obtained neglecting spalling are similar to the results obtained taking spalling into account.

Similar conclusions are obtained from comparing the stresses in the bulk with and without spalling. Thus, if no stirrups are considered and apart from the expansion of the steel cross section, no significant differences are found due to spalling, either at the bulk or at the steel-concrete interfaces. In fact, the volume expansion occurs without any important restraint introduced by the boundary conditions, such that the stresses are not significantly altered.

In order to take into account the observed longitudinal cracking along the reinforcement due to spalling, option (b) is adopted.

In this case, the volume expansion is not introduced at the steel bar; instead, it is *transferred* to the interfaces above and below the reinforcement. This is done by introducing splitting forces directly at the interfaces during the corrosion stage. These forces are adjusted such that they enforce a normal opening of the interface w_n^{eq}, defined according to:

$$w_n^{eq} = w_n^{spalling} \cdot c_w, \tag{4}$$

where

$$w_n^{spalling} = \varepsilon_{yy}^{corrosion} \times \phi, \tag{5}$$

ϕ is the bar diameter and c_w is a coefficient which accounts for the variation of the crack opening w_n across the width (see part I). At both interfaces below and above the reinforcement bar, half of w_n^{eq} is adopted during the corrosion stage. Given the maximum corrosion level $\eta = 20\%$, we obtain $w_n^{spalling} = (\sqrt{1.2} - 1) \times 16 = 1.53$ mm. The adopted equivalent normal opening is $w_n^{eq} = 1$ mm, leading to $c_w = 0.65$ (see appendix E).

This w_n^{eq} value is introduced step by step during the corrosion stage. The splitting forces are controlled such that w_n^{eq} is enforced at the location where the maximum normal jump displacement at the interface is obtained. As a consequence, a uniform stress state is enforced along the interface due to the splitting forces. In this way larger values of equivalent normal opening w_n^{eq} are automatically obtained near the most damaged zones along the length of the beam (see part I).

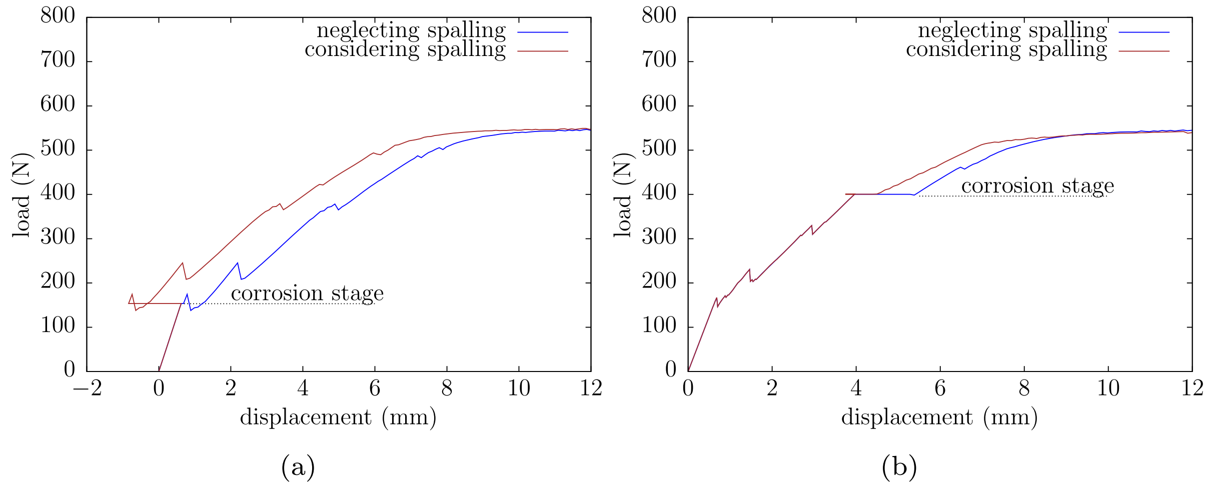

Fig. 20 Load-displacement curves obtained in case 1 (F_1 =153 N) (a) and case 2 (F_1 =400 N) (b), without and with spalling / volume expansion

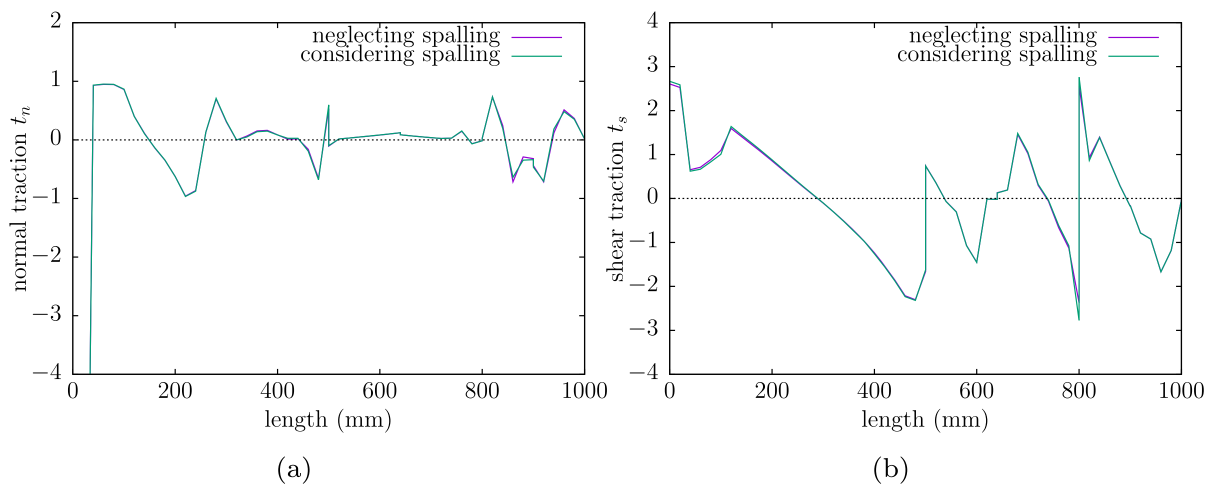

Fig. 21 Normal traction (a) and shear traction (b) distribution obtained along the length of the beam, at the end of the corrosion stage, at the bottom steel-concrete interface in loading case 1 (F_1 =153 N), without and with spalling

In each iteration the splitting forces change due to the increase of damage at the interface. In all the examples presented in this Section, a mode-II damage driving mechanism with no prescribed return mapping is adopted (item ii) in Section 3.3). This is due to the fact that, during the iterative process while introducing the splitting forces, the normal traction and the shear traction become out of proportion. As a consequence, radial return mapping is inappropriate in this case.

In Figs. 23a and 23b , the load-displacement results obtained when considering spalling as an interface expansion (option b) are presented, for each level of the pre-corrosion load. In this case the displacement measured at midspan at the top of the beam does not decrease during the corrosion stage since there is no volume expansion; in fact, an increase of the displacement is observed during corrosion compared to the non spalling case. As a consequence, considerable more damage is obtained at the corrosion stage in the solution obtained with splitting forces, when compared to the solution obtained without spalling.

In Figs. 24 and 25, the deformed meshes corresponding to Figs. 23a and 23b, respectively, are shown. In these Figures, detachment of the cover at some zones

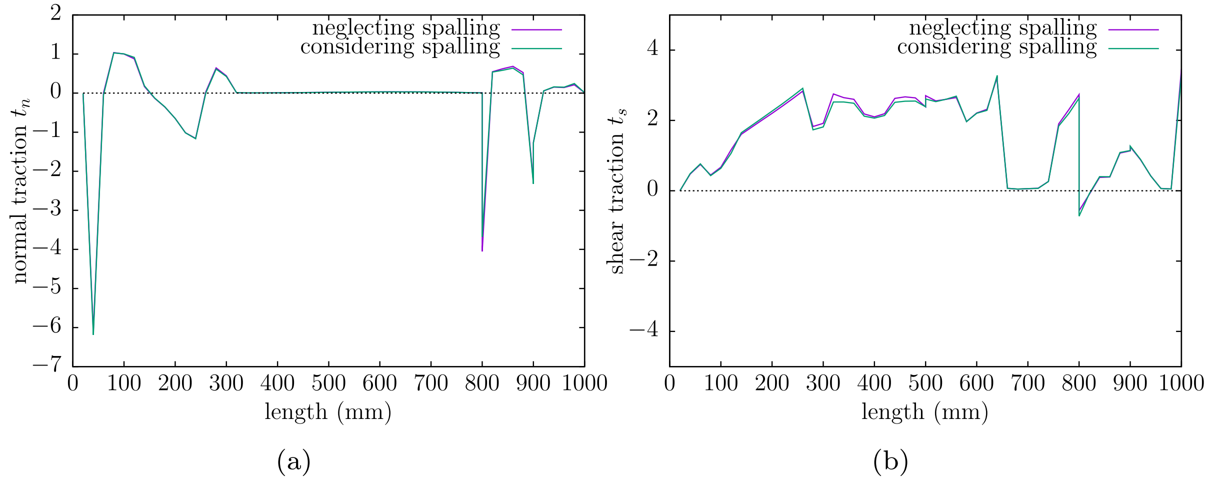

Fig. 22 Normal traction (a) and shear traction (b) distribution obtained along the length of the beam, at the end of the corrosion stage, at the upper steel-concrete interface in loading case 1 (F_1 =153 N), without and with spalling

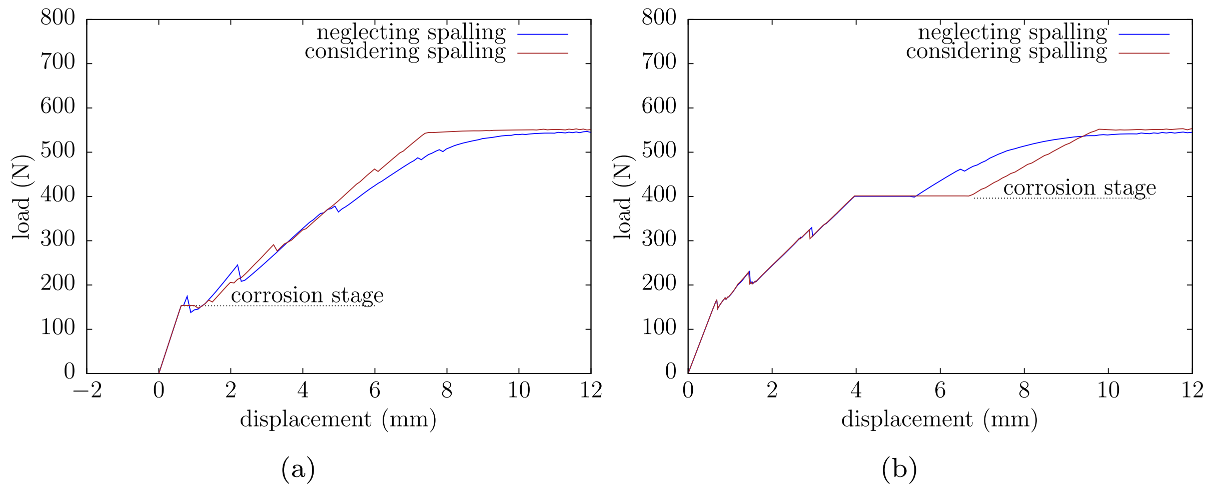

Fig. 23 Load-displacement curves obtained in case 1 (F_1 =153 N) (a), and case 2 (F_1 =400 N) (b), without and with spalling/ splitting forces

Fig. 24 Deformed mesh obtained at the end of the test with spalling (F_1 =153 N, amplification displacement factor = 10)

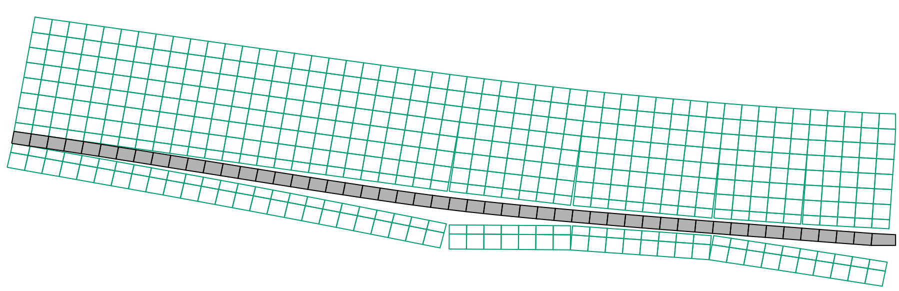

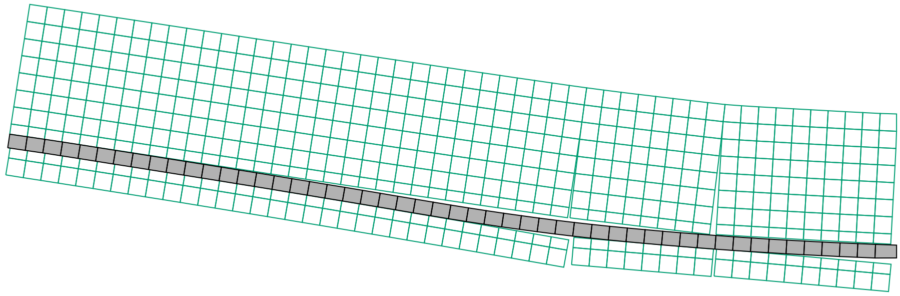

Fig. 25 Deformed mesh obtained at te end of the test with spalling (F_1 =400 N, amplification displacement factor = 10)

is clear, specially under loading case 1, where corrosion is already present in earlier stage. In both cases, it is also possible to observe the detachment of the steel reinforcement at the upper steel-concrete interface.

The splitting forces give rise to a separation between steel and concrete and to a damage increase in the normal direction. However, the bond-slip relationship remains mostly unaffected by the splitting forces. In fact, according to the limit surface (see Fig.1 in part I), a decrease of the normal traction leads to an increase of the bond strength, not the other way around. Thus, similar to the volume expansion case (a), in the tests presented in Figs.23a to 25, the bond slip relationship is essentially controlled by the degradation introduced by the corrosion stage, as done in the previous Sections 3.1 to 3.3.

In the following tests, the bond slip relationship at the steel-concrete interface is also considered a function of the normal opening, as mentioned in part I. It is assumed that the bond strength decays linearly with w_n to a residual vale c_{res} when the normal opening is equal to $w_n^{lim} = (54/15) \times (G_F/f_t)$[3]. We get, $w_n^{lim} = 3.6 \times 0.1/3 = 1.2$ mm. A residual cohesion value of $c_{res} = 0.5$ MPa is assumed.

In Figs. 26a and 26b the load displacement curves obtained with splitting forces in Figs. 23a and 23b are compared to the load displacement curves obtained considering the dependence of the bond strength on the normal opening of the steel concrete interface.

In Figs. 27 and 28, the deformed meshes corresponding to Figs. 26a and 26b,are shown, respectively.

No major differences are found in the load displacement curves obtained either neglecting or considering the bond dependence on the normal opening of the steel concrete interface. In Fig. 26a a larger displacement is found at the corrosion stage in the latter case.

However, in Figs.27 and 28, the detachment of the steel bar is both more pronounced and widely distributed along the bar than in Figs. 24 and 25, both above and underneath the bar. In the following tests performed with splitting forces, the dependence of the bond strength on the normal opening of the steel concrete interface is taken into account.

During the simulations, at the corrosion stage, the nonlinear structural behaviour is due to cracking and tension stiffening, both dependent on the degree of corrosion. Later, nonlinear concrete behaviour under compression and yielding of the steel reinforcement are responsible for the transition to the *plateau* corresponding to the ultimate load. In the load displacement curves obtained with spalling modelled by splitting forces, a more abrupt stiffness decrease is found close to the ultimate load, when compared to the tests with volume expansion. In all the tests with spalling - modelled with either volume expansion or splitting forces - the same concrete elements attain the maximum compressive stress f_{ck}. These elements are located at the top of the beam, adjacent to the symmetry line and next to the main two other cracks observed in Fig. 17. In the tests corresponding to spalling modelled with splitting forces, the evolution of damage in these elements occurs later and is less pronounced, when compared to the volume expansion tests. As a consequence, in the tests obtained with splitting forces, the effect of the yielding of the steel reinforcement at midspan is the main cause for structural damage close to the ultimate load.

However, the maximum load is approximately the same in both cases, since it is dominated by the concrete and steel strength (f_{ck}, f_{yk})[4], as long as the rein-

[3] In a bilinear softening relation the normal displacement jump corresponding to the transition to a stress free crack is equal to $w_n^{lim} = (54/15) \times (G_F/f_t)$.

[4] Recall that compressive softening is not taken into account since elastoplastic behaviour is adopted under compression.

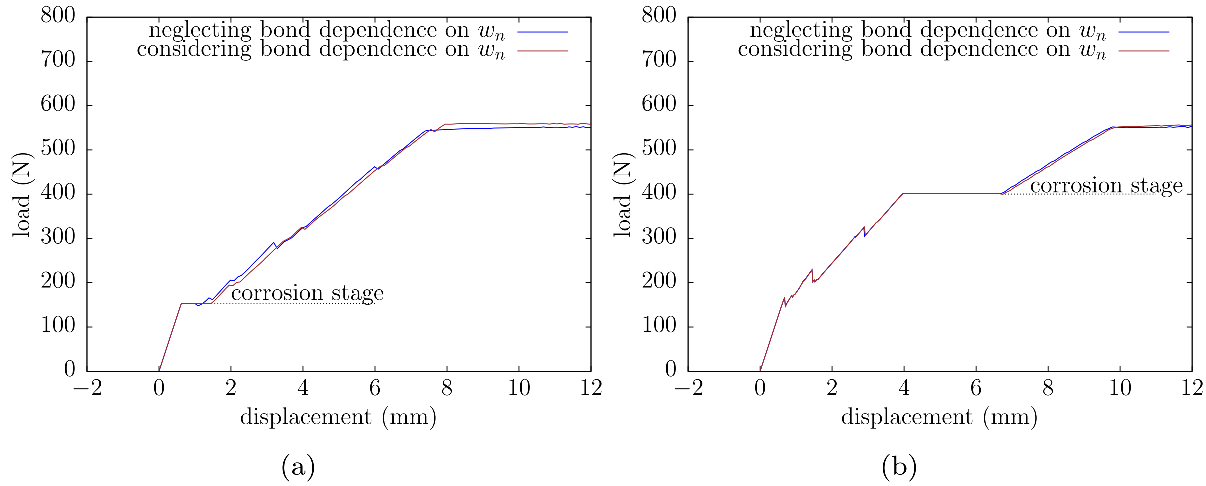

Fig. 26 Load-displacement curves obtained in case 1 (F_1 =153 N) (a), and case 2 (F_1 =400 N) (b), without and with spalling/ splitting forces, considering the dependence of the bond strength on the normal opening of the steel concrete interface

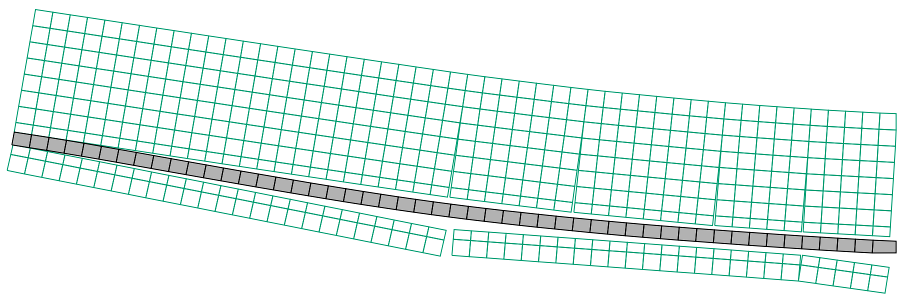

Fig. 27 Deformed mesh obtained at the end of the test with spalling (F_1 =153 N, amplification displacement factor = 10), considering the dependence of the bond strength on the normal opening of the steel concrete interface

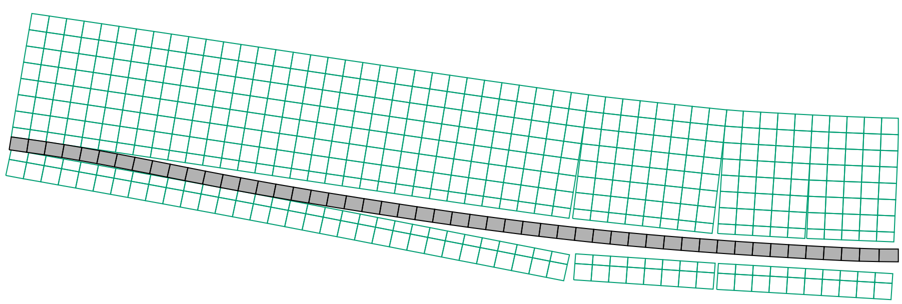

Fig. 28 Deformed mesh obtained at the end of the test with spalling (F_1 =400 N, amplification displacement factor = 10), considering the dependence of the bond strength on the normal opening of the steel concrete interface

forcement anchorage is not significantly damaged (see Section 3.7).

3.5 Stirrup confinement

In Fig. 29, the adopted mesh including compressive reinforcement and stirrups is presented. The compressive reinforcement consists of $2\phi 10$ and is introduced by means of truss elements located at 180 mm height, with perfect bond assumed between steel and concrete. The stirrups consist of $S\phi 10$ and are introduced in the mesh by truss elements at several locations along the beam (stirrup spacing is $s \in [8 : 16]$ cm):

20	100	200	320	460	600	760	920

Location of stirrups along half the length of the beam (mm)

Perfect bond is also assumed between the stirrups and the concrete. The stirrups envelope both the compressive and the tensile steel reinforcement. In appendix C, it is shown that the design shear force is much lower than the design shear resistance.

First the load-displacement results obtained with spalling from volume expansion, with and without stirrups, are compared in Figs. 30a and 30b . In Figs. 31a and 31b , spalling obtained from splitting forces is taken into account.

Note that, in all examples shown in Figs.30a , 30b and 31a , 31b , the same ultimate load is reached asymptotically, being essentially defined by yielding of the longitudinal steel reinforcement. The differences between tests performed with volume expansion of the steel bar and with splitting forces are that, in the former case, the pre-ultimate load obtained with stirrups is above the load obtained without stirrups, whereas the opposite occurs in the latter case. In the tests presented in Figs. 31a and 31b , a stiffness decrease before the ultimate load is reached with stirrups when compared to the tests without stirrups. Similar to the observation made in the previous Section, in the tests with stirrups, the nonlinear behaviour of concrete under compression is attained earlier, leading to a global stiffness decrease. This is one of the effects of stirrup confinement, which gives rise to the increase of compressive stresses at the top of the beam. Nevertheless, plastic failure is still achieved in all cases, due to the yielding of the steel and not due to concrete crushing under compression.

With stirrups, no important differences are found taking into account the dependence of the bond strength on the normal opening of the steel concrete interface.

In Figs. 32 and 33, the deformed meshes corresponding to Figs. 31a and 31b , respectively, are shown. Compared to the deformed meshes obtained without stirrups (Figs. 24 and 25), it is clear that the steel-concrete interface above the reinforcement is now closed, although detachment of the cover remains.

Important differences are also found at local level. In Figs. 34a and 34b , the shear traction distribution obtained a the bottom steel-concrete interface, along the length of the specimen, is presented with and without stirrups. In the former case (a), spalling is obtained from volume expansion, whereas in the latter case (b), spalling is obtained with splitting forces. These results were obtained at the end of the corrosion stage in loading case 1.

The effect of the stirrups is obvious: in (a), at each stirrup location, the shear traction drops to zero. This is due to the fact that high tensile normal tractions develop at these locations under mixed-mode (case 2.(c) in Table 4). According to the proposed limit surface, the normal traction is limited to the tensile strength ($f_t = 3$ MPa) and the shear strength is lost (see Fig.1 in part I). Thus, the stirrup confinement applied to the structure within the height of the stirrups, gives rise to the loss of adhesion underneath the stirrup location. In fact, it is found that all stirrups are stretched and reach the yield stress at the bottom, due to the expansion of the main reinforcement cross section. However, this effect may be overestimated since the accumulation of corrosion products, which are less stiff than the core of the steel, may not give rise to such large increase of strain in the stirrups.

In case (b), the stirrups are not stretched since no volume expansion occurs in the horizontal bars. As a consequence, no large concentrated tensile tractions are observed at the lower steel-concrete interface. Nevertheless, this effect is still present although distributed along the length of the beam. This is why, due to mixed-mode fracture, the bond traction obtained with stirrups consistently lies below the corresponding bond traction obtained without stirrups.

Similar conclusions are obtained in loading case 2, as shown in Figs. 35a and 35b . In case (a), locally, at the stirrup location ($x = 100, 200, 320, 460, 600, 760, 920$ mm), the bond traction drops to zero. In case (b) no traction drop at the stirrup locations is observed.

In Figs. 36a to 37b , the traction distribution ot the upper steel-concrete interface is presented for both situations (a) - spalling due to volume expansion and (b) - spalling due to splitting forces. These Figures correspond to loading case 1 (F_1 =153 N). In Fig. 36a, the distribution of the normal traction along the length of the specimen is presented. The effect of stirrup confinement is clear, with high compressive tractions developing at the stirrup location. Again, these high values are related to the expansion of the steel cross section and may be exaggerated due to the reduced stiffness of the expansion products. In Fig. 36b , the normal tractions are always such that $t_n \in [-1 : 1]$ MPa, since no volume expansion occurs.

In Fig. 37a the distribution of the bond traction at the upper steel-concrete interface, along the length of the specimen is shown. A slight increase of the bond traction is observed in the results obtained with stirrups at the corresponding location. These *peak* values are related to the normal compressive traction due to the stirrup confinement observed in Fig. 36a (case 2.(b)

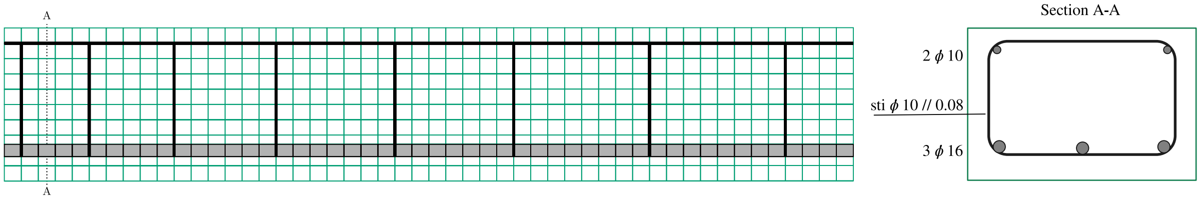

Fig. 29 Mesh (half of the specimen) and cross section of the beam

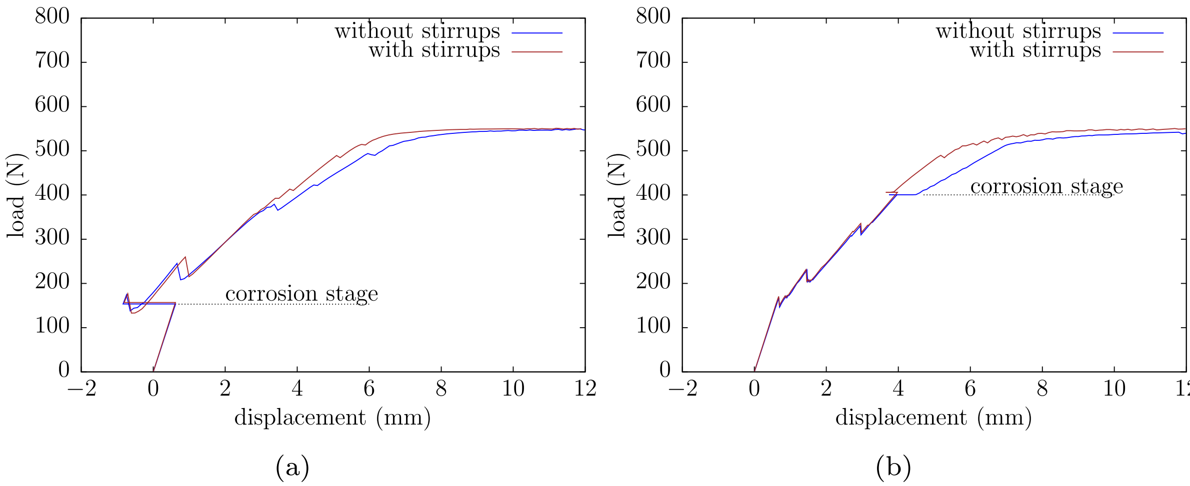

Fig. 30 Load-displacement curves obtained in cases 1 (F_1 =153 N) (a) and case 2 (F_1 =400 N) (b), without and with stirrups, considering spalling with volume expansion

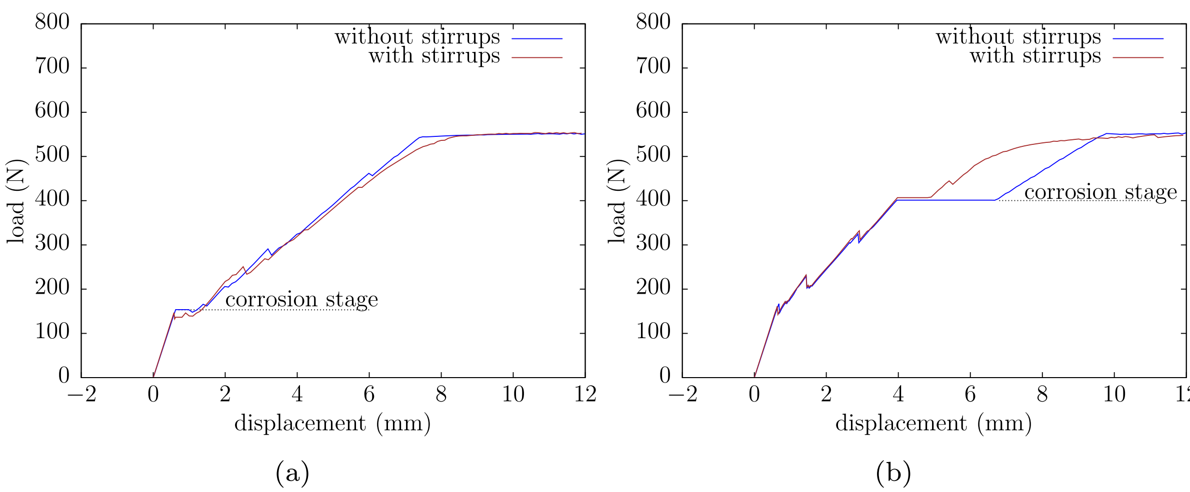

Fig. 31 Load-displacement curves obtained in loading case 1 (F_1 =153 N) (a) and loading case 2 (F_1 =400 N) (b), without and with stirrups, considering spalling with splitting forces

in Table 4). In Fig. 37b the bond traction distribution obtained with corrosion by splitting forces is presented. The *peak* values are no longer present at the stirrup locations. In this case, the effect of stirrup confinement gives rise to a regularization of the bond traction distribution along the length of the beam.

Fig. 32 Deformed mesh obtained at the end of the test with spalling/ splitting forces (F_1 =153 N, amplification displacement factor = 10)

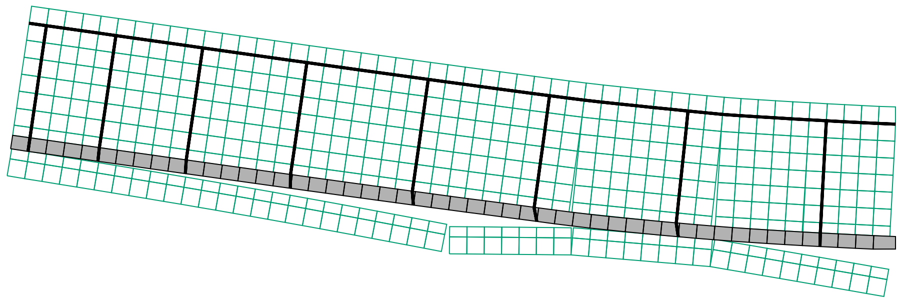

Fig. 33 Deformed mesh obtained at the end of the test with spalling/ splitting forces (F_1 =400 N, amplification displacement factor = 10)

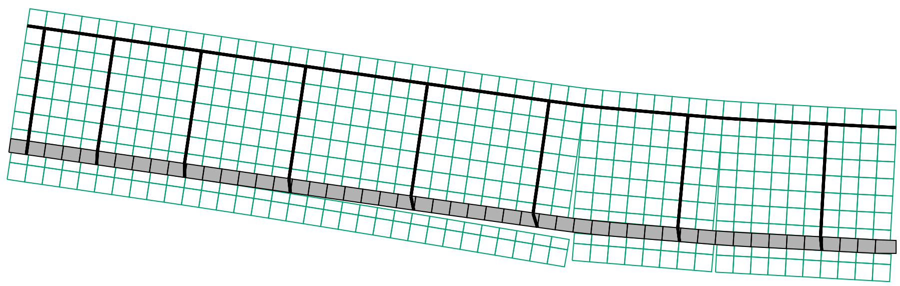

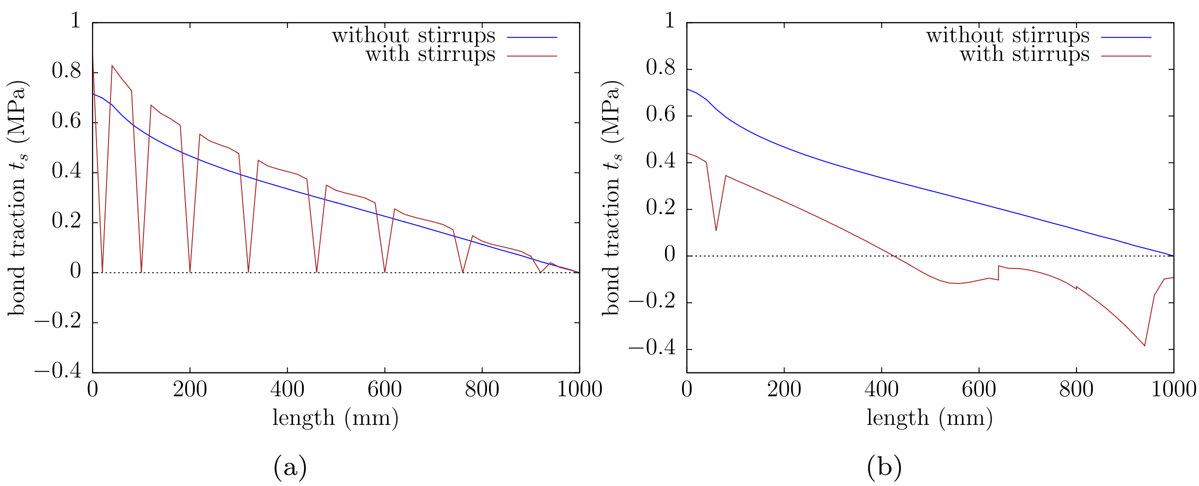

Fig. 34 Shear traction distribution along the length of the beam at the bottom steel-concrete interface, taking spalling into account, at the end of the corrosion stage, without and with stirrups, in case 1 (F_1 =153 N): (a) spalling with volume expansion, (b) spalling with splitting forces

In Figs. 38a and 38b , the distribution of the maximum principal stress component σ_I obtained in the main reinforcement steel is plotted for loading case 1 ($F_1 = 153$ N). Three solutions are considered: i) no spalling, ii) spalling without stirrups and iii) spalling with stirrups.

Equivalent comparisons are presented in Figs. 39a and 39b for loading case 2 ($F_1 = 400$ N).

In general, similar results are obtained with and without stirrups, either neglecting or considering the effect of spalling. It is concluded that cracks located at $x = 0.8$ m and midspan always open. In all cases it can also be observed that the crack located at $x = 900$ mm does not fully open, as stated in Section 3.3. With stirrups higher stresses are found at the neighbourhood of the crack located at $x = 0.64$ m, attaining the yield value in Figs. 38a , 39a and 39b . In Fig.39b higher

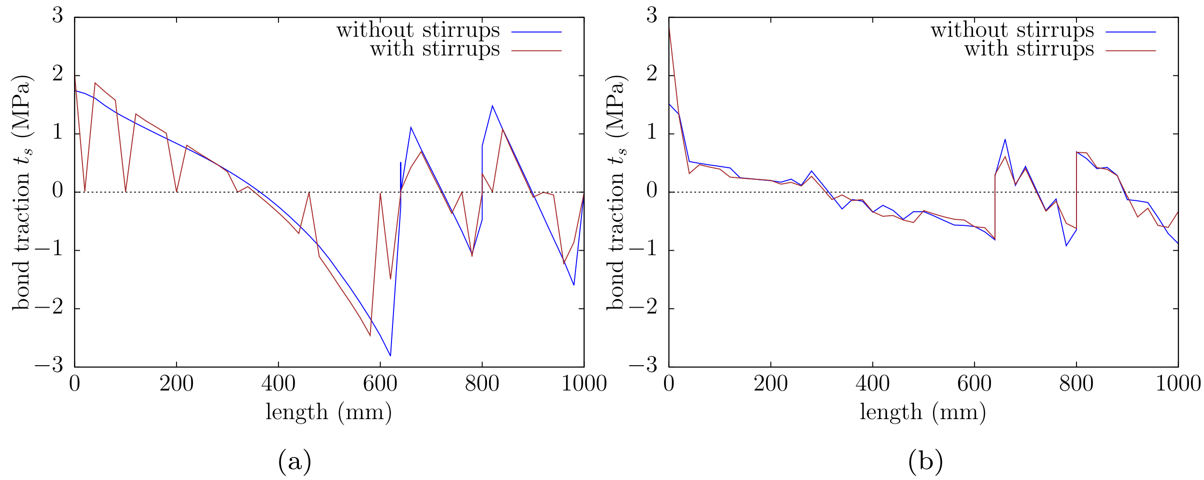

Fig. 35 Shear traction distribution along the length of the beam at the bottom steel-concrete interface, taking spalling into account, at the end of the corrosion stage, without and with stirrups, in case 2 (F_1 =400 N):)(a) spalling with volume expansion, (b) spalling with splitting forces

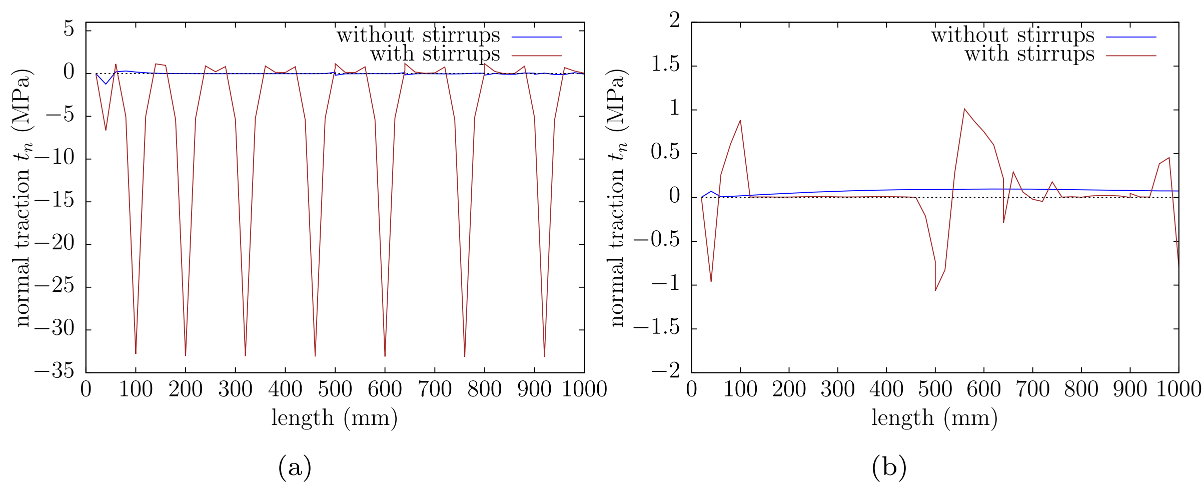

Fig. 36 Normal traction distribution obtained along the length of the beam at the upper steel-concrete interface in case 1 (F_1 =153 N), at the end of the corrosion stage, without and with stirrups; (a) spalling with volume expansion, (b) spalling with slitting forces

steel stresses are found close to the anchorage in the tests performed taking spalling into account. In these two tests, crack does not open at $x = 0.5$ m as can be observed in Figs. 25 and 33. As a consequence, the steel stress at this location drops, giving rise to an increase of the stress between the anchorage and midspan.

It is interesting to observe that, depending on the steel-concrete bond distribution along the specimen, different tension stiffening mechanisms develop, giving rise to dominant cracks at different locations.

3.6 Corrosion introduced at the centre of the beam

Now it is assumed that corrosion is introduced at the central zone of the beam only. This can happen due to the fact that the main cracks occur at this central zone, making it easier for the moisture to induce corrosion locally (Silva 2018). The central zone is defined by $x \in [0.64 : 1.36]$ m. All previous effects are considered, namely bond stiffness degradation, core reduction, dependence of the bond traction on the normal traction and spalling. In the following, results with and

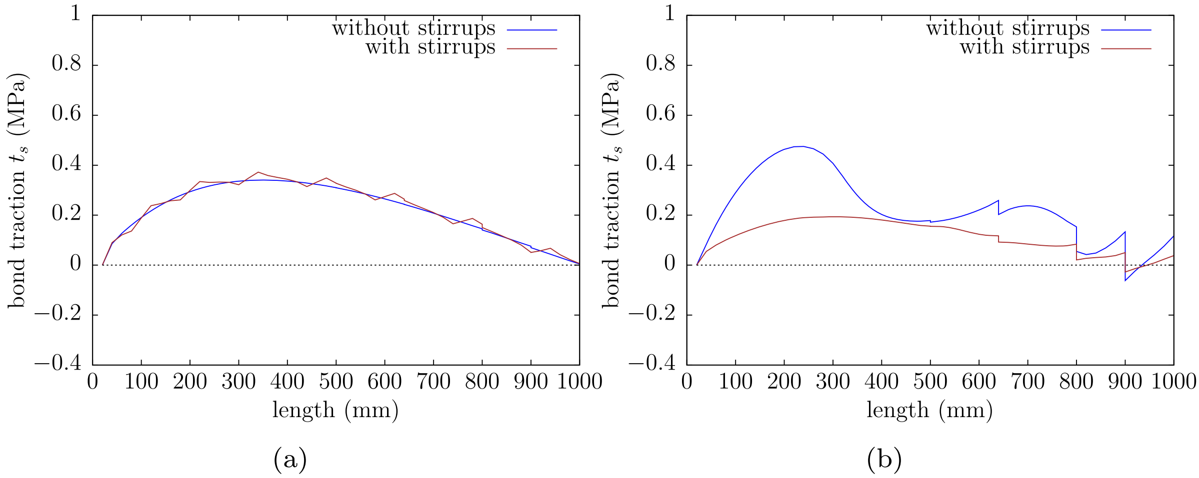

Fig. 37 Shear traction distribution obtained along the length of the beam at the upper steel-concrete interface in case 1 (F_1 =153 N), at the end of the corrosion stage, without and with stirrups; (a) spalling with volume expansion, (b) spalling with slitting forces

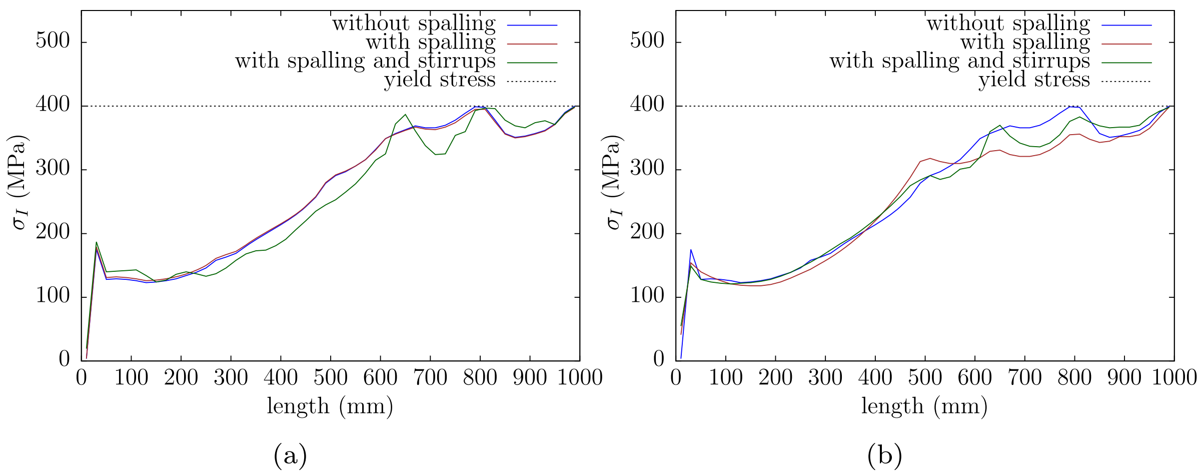

Fig. 38 Distribution of σ_I obtained at the main steel reinforcement in loading case 1 (F_1 =153 N), without spalling, with spalling and with spalling and stirrups: (a) spalling with volume expansion, (b) spalling with splitting forces

without stirrup confinement are compared. Considering half of the beam due to symmetry, we have: $\eta = 0$ for $x \in [0.00 : 0.64]$ m, $\eta = 20\%$ for $x \in [0.64 : 1.00]$ m.

First, spalling is taking into account under volume expansion. In Fig. 40a , the load displacement curve obtained with corrosion along the whole length of the beam is compared to the load-displacement curve obtained with corrosion localized at the central zone.

In Fig. 41, the deformed mesh obtained at the end of the test with corrosion localized at the central zone is presented for loading case 1 ($F_1 = 153$ N).

It can be observed that the solution with corrosion in the central zone exhibits more damage, with corresponding stiffness decrease, which is essentially due to crack opening at the transition zone from $\eta = 0$ to $\eta = 20\%$. The ultimate load remains the same, due to the yielding of the reinforcement steel, which means that bond between steel and concrete is still sufficient to transmit the stresses to the reinforcement.

In Fig. 40b , the load displacement curve presented in Fig. 40a , with corrosion localized at the central zone of the beam, is compared to the load displacement curve obtained with stirrups. In Fig. 42, the corresponding deformed mesh obtained with stirrups is shown.

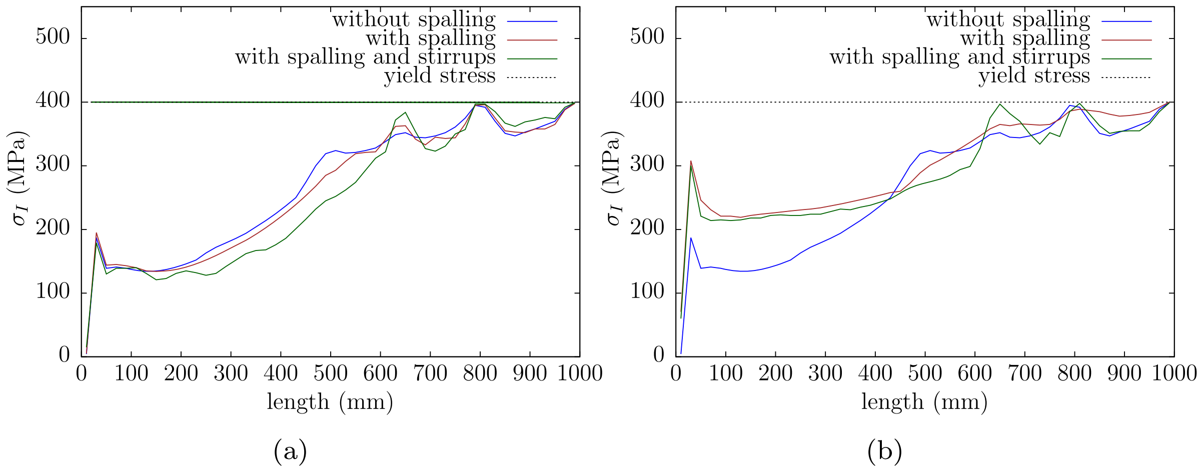

Fig. 39 Distribution of σ_I obtained at the main steel reinforcement in loading case 2 (F_1 =400 N), without spalling, with spalling and with spalling and stirrups: (a) spalling with volume expansion, (b) spalling with splitting forces

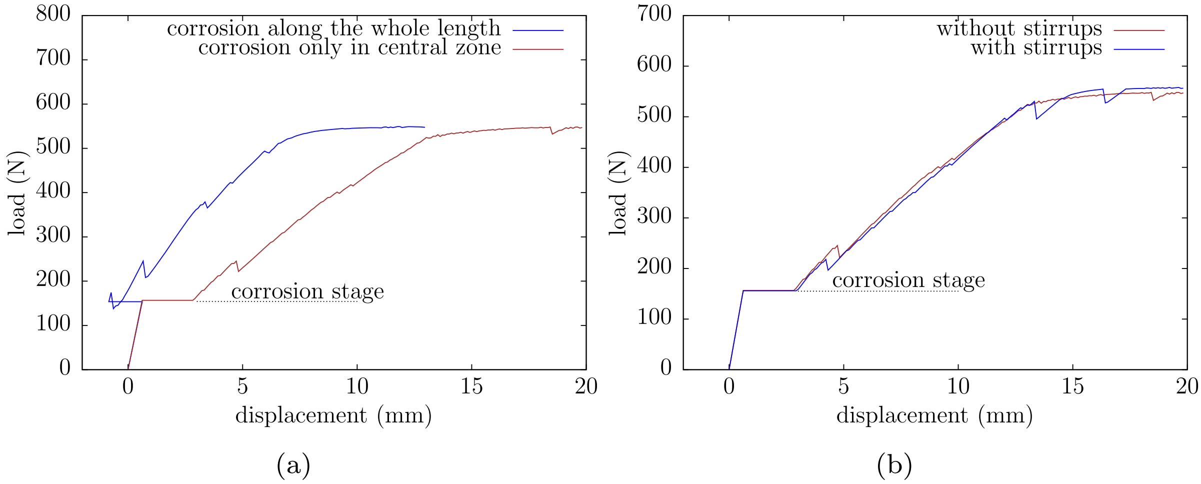

Fig. 40 Load-displacement curves with corrosion along the whole length of the beam and with corrosion localized at the central zone of the beam, (a) without stirrups, (b) with stirrups (case 1, F_1 = 153 N)

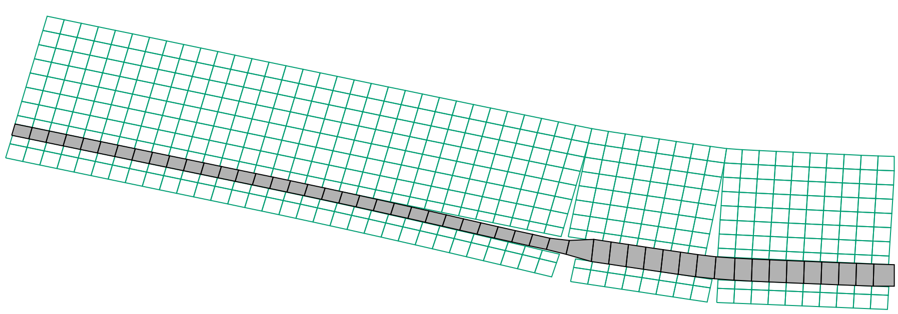

Fig. 41 Deformed mesh obtained at the end of the test, with corrosion localized at the central zone (case 1, F_1 = 153 N, displacement amplification factor 10)

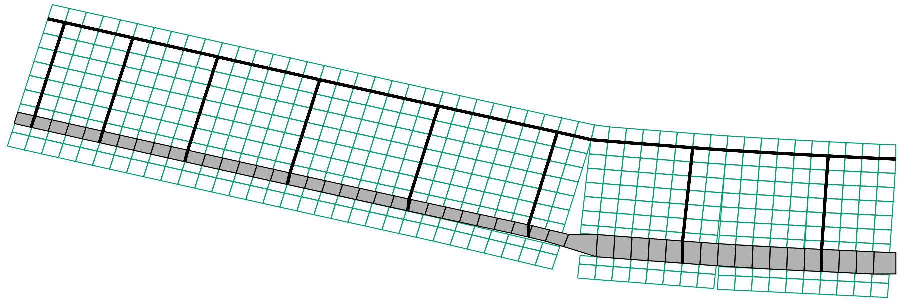

Fig. 42 Deformed mesh obtained at the end of the test, with corrosion localized at the central zone and stirrups (case 1, $F_1 = 153$ N, displacement amplification factor 10)

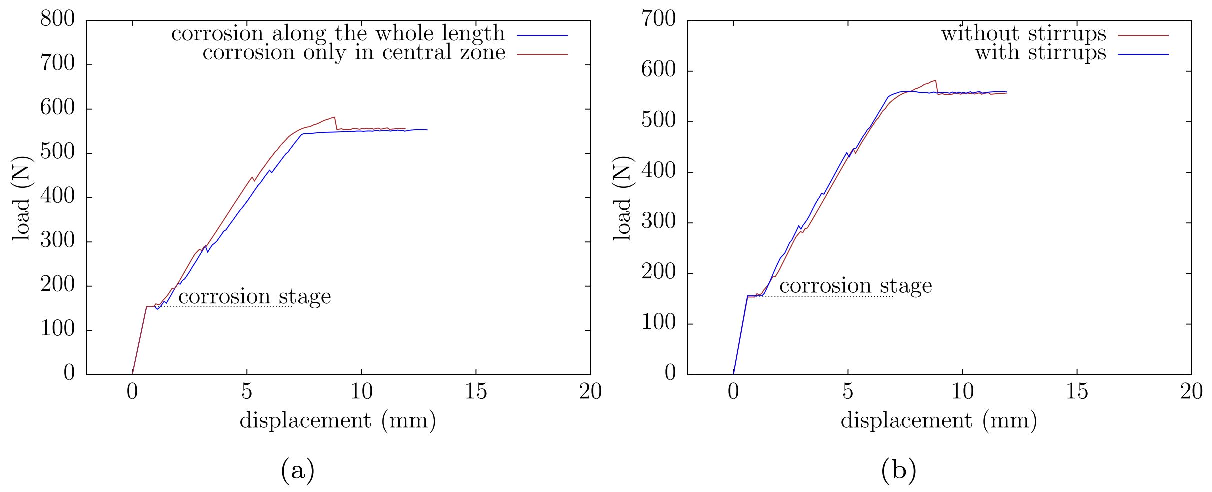

Fig. 43 Load-displacement curves with corrosion along the whole length of the beam and with corrosion localized at the central zone of the beam, (a) without stirrups, (b) with stirrups (loading case 1, $F_1 = 153$ N)

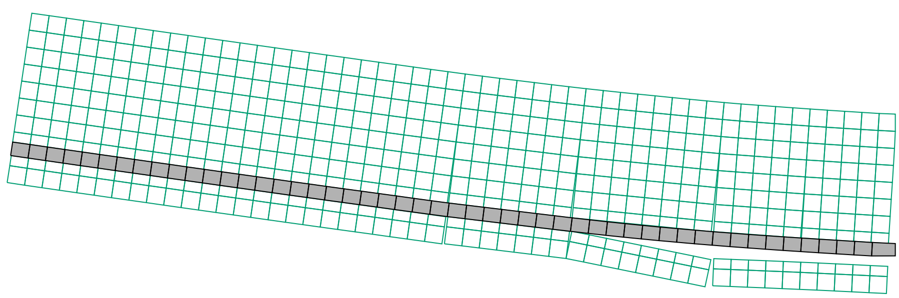

Fig. 44 Deformed mesh obtained at the end of the test, with corrosion localized at the central zone (loading case 1, $F_1 = 153$ N, displacement amplification factor 10)

Thus, in the solutions obtained with volume expansion, the corrosion stage gives rise to a *plateau* at the load level, with a large increase of the displacement, in spite of the expansion of the steel cross section. Moreover, after the corrosion stage the stiffness is much smaller in the example with corrosion localized at the central zone of the beam. This is due to localization of damage at the transition zone from $\eta = 0$ to $\eta = 20\%$, as can be seen in the deformed meshes presented in Figs. 41 and 42. Similar conclusions are obtained in loading case 2, as shown in Figs. 46, 47a to 48.

Now the second approach for spalling with splitting forces at the steel concrete interface is introduced. In Fig. 43a , the load displacement curve obtained with corrosion along the whole length of the beam is compared to the load-displacement curve obtained with corrosion localized at the central zone.

In Fig. 44, the deformed mesh with corrosion introduced at the central zone of the beam is shown.

In Fig. 43b , the load displacement curve presented in Fig. 43a , with corrosion at the central zone of the beam, is compared to the load displacement curve obtained

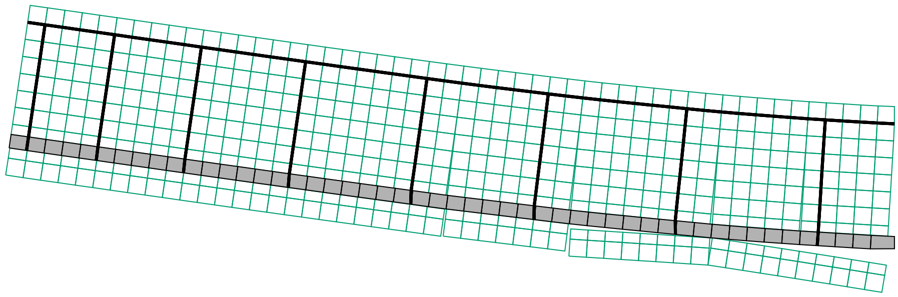

Fig. 45 Deformed mesh obtained at the end of the test, with corrosion localized at the central zone and stirrups (loading case 1, $F_1 = 153$ N, displacement amplification factor 10)

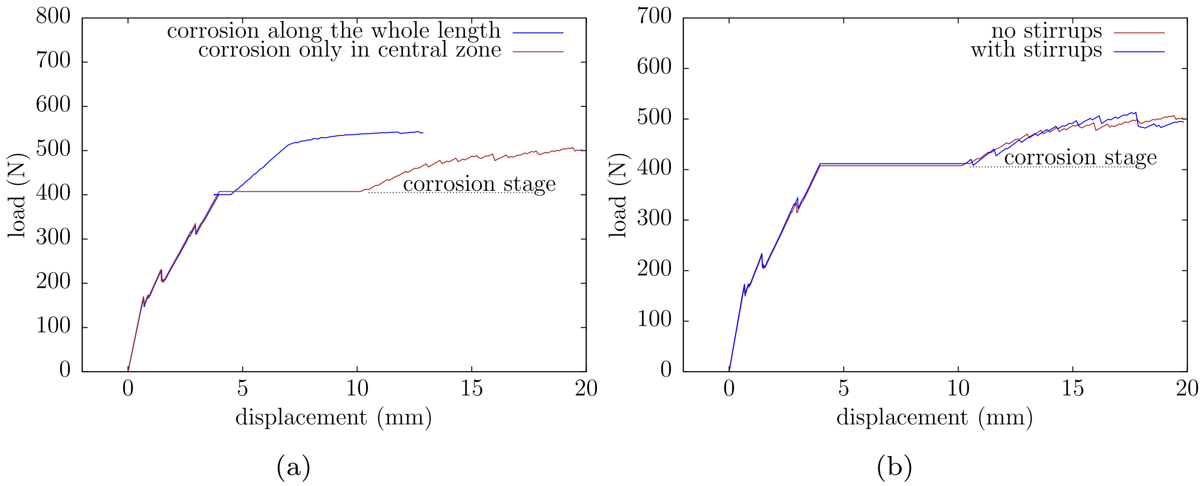

Fig. 46 Load-displacement curves with corrosion along the whole length of the beam and with corrosion localized at the central zone of the beam, (a) without stirrups, (b) with stirrups (loading case 2, $F_1 = 400$ N)

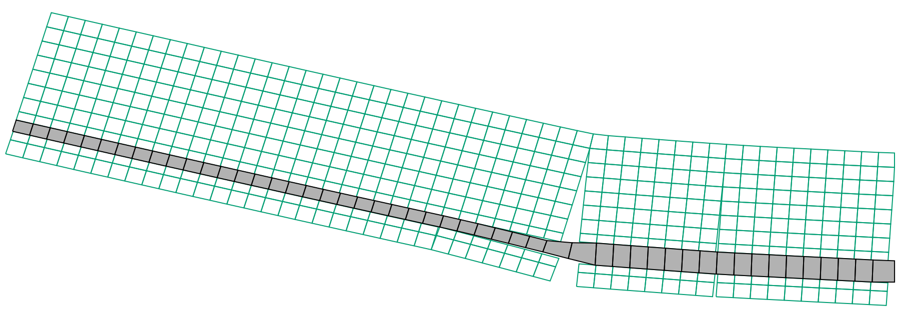

Fig. 47 Deformed mesh obtained at the end of the test, with corrosion localized at the central zone (loading case 2, $F_1 = 400$ N, displacement amplification factor 10)

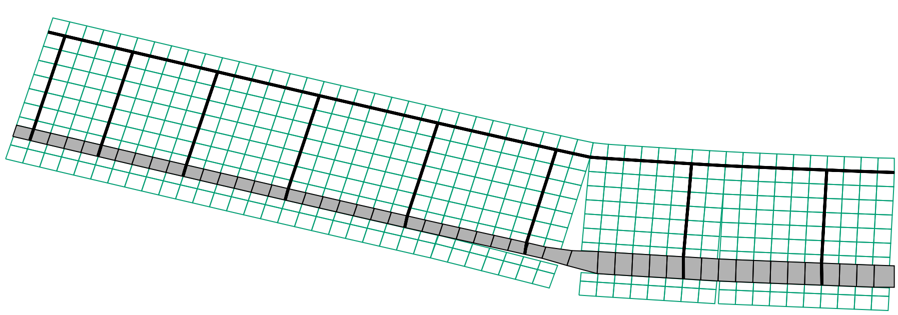

Fig. 48 Deformed mesh obtained at the end of the test, with corrosion localized at the central zone and stirrups (loading case 2, $F_1 = 400$ N, displacement amplification factor 10)

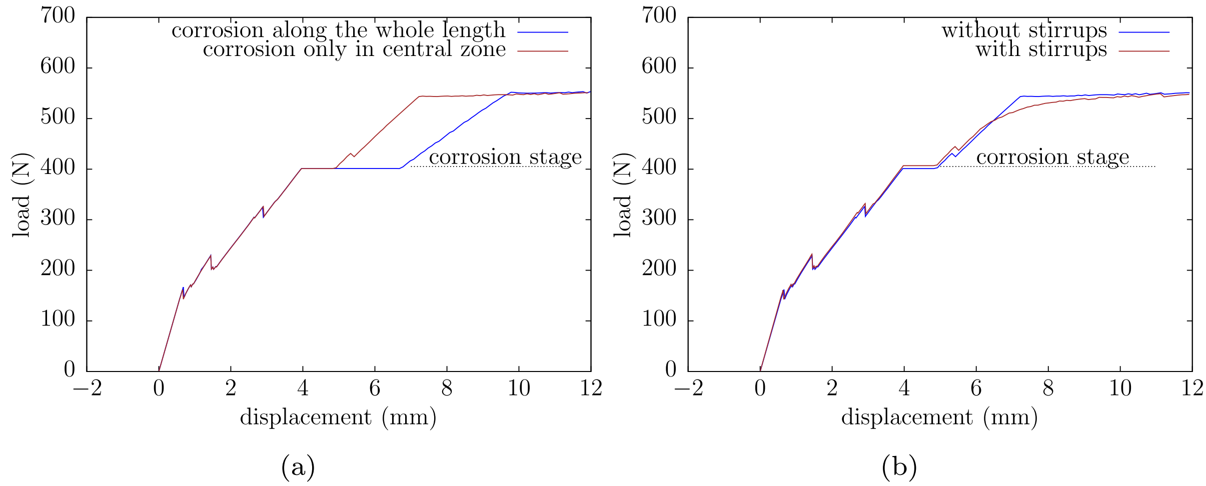

Fig. 49 Load-displacement curves with corrosion along the whole length of the beam and with corrosion localized at the central zone of the beam, (a) without stirrups, (b) with stirrups (loading case 2, $F_1 = 400$ N)

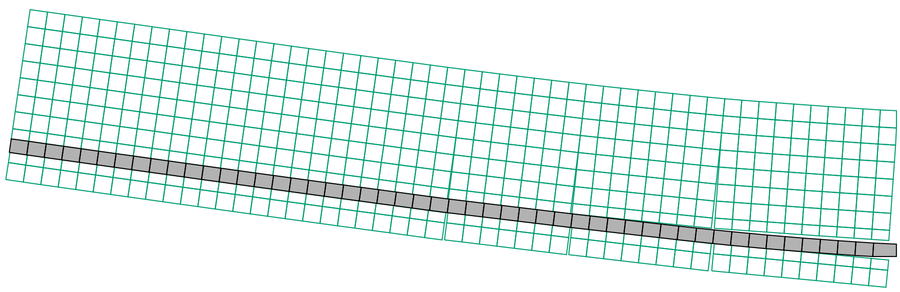

Fig. 50 Deformed mesh obtained at the end of the test, with corrosion localized at the central zone (loading case 2, $F_1 = 400$ N, displacement amplification factor 10)

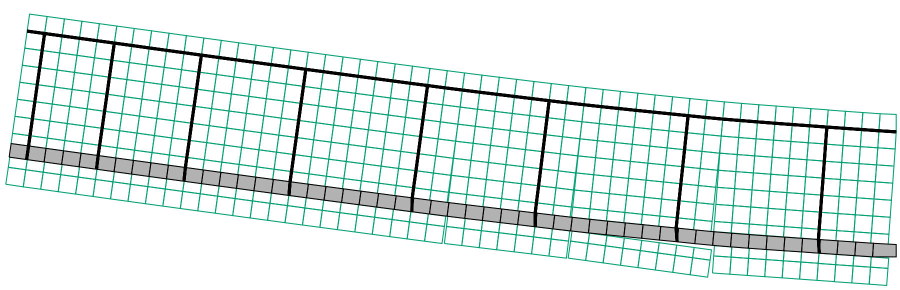

Fig. 51 Deformed mesh obtained at the end of the test, with corrosion localized at the central zone with stirrups (loading case 2, $F_1 = 400$ N, displacement amplification factor 10)

with stirrups. In Fig. 45, the corresponding deformed mesh obtained with stirrups is shown.

In Figs. 49, 50a to 51, results corresponding to loading case 2 are presented.

Introducing spalling with splitting forces, localization of damage at the transition zone does not occur. As a consequence, the stiffness in the load displacement curves does not differ much and a decrease of the displacement at the corrosion stage is found, which is more pronounced in loading case 2 (Fig.49a). Under loading case 1, in the result obtained without stirrups and corrosion at the central zone a slightly stiffer solution is obtained (Fig.43a). However, with stirrups this difference vanishes (Fig.43b).

Nevertheless, the effect of the corrosion at the central zone of the beam is notorious in the deformed meshes presented in Figs. 44 and 45; conversely to Figs. 24 and 32, splitting of the cover now occurs at $x > 0.64$ m.

From the viewpoint of the degradation of the bond-slip relationship due to corrosion, the results obtained with splitting forces seem more realistic. The results obtained with volume expansion give rise to a fracture

Table 1 Initial and final multilinear mode-II fracture relationships adopted for bond-slip

Initial bond-slip law		Final bond-slip law	
w_s (mm)	t_s (MPa)	w_s (mm)	t_s (MPa)
0.20	6.371	0.20	2.159
0.617	8.749	0.42	1.565
1.5	7.397	1.5	0.816
2.0	6.547	5.0	0.200
2.5	5.791	15.0	0.000
5.0	3.136		
15.0	0.270		
30.0	0.000		

localisation at the transition zone, which also seems realistic. However, the high stiffness decay in this case seems exaggerated, since the solution obtained with corrosion at a localised zone of the beam exhibits more damage than the solution obtained with corrosion along the whole length of the beam.

3.7 Slippage of the anchorage zone

In this Section, the effect of the slippage of the anchorage is analyzed. For this purpose, the steel-concrete interface at the left edge of the beam, which is assumed very stiff in the previous tests in order to simulate the anchorage, is now treated equally to the others. Corrosion is considered along the whole length of the beam.

Similar to the work presented in Alfaiate et al. (2023), it is found that the effect of a deficient anchorage can not be detected simply by releasing the stiffness of the first steel-concrete interface. In fact, if the steel bar is allowed to slip at the anchorage zone, the bond strength is distributed along the whole length of the steel-concrete interface and may still withstand the full load.

Thus, the consequence of a deficient anchorage can only be detected by exaggerating the level of corrosion. For that purpose, the residual bond-slip law defined in Table 1 is adopted ($G_F^{II} = 4.47$ N/mm, Silva (2018)). In order to maintain the steel strength constant compared to the previous tests, this high degree of corrosion is only applied to the bond-slip relationship. Both the core reduction and the expansion of the steel cross section corresponding to corrosion level $\eta = 20\%$ are kept constant. Only loading case 1 is considered ($F_1 = 153$ N).

In Fig. 52a the load-displacement curve obtained with a stiff anchorage is compared to the load-displacement curve obtained applying the final bond-slip law from Table 1 to the whole steel-concrete interface. Both tests are performed without stirrups and spalling is introduced with volume expansion of the reinforcement.

In Fig. 53 the deformed mesh obtained at the end of the test is presented. The loss of adhesion at the anchorage zone is clear.

In Fig. 52b the load-displacement curve obtained with a stiff anchorage is compared to the load-displacement curve obtained applying the final bond-slip law from Table 1 to the whole steel-concrete interface. In this case, stirrups are taken into account and spalling is introduced with splitting forces. In this case, dependence of the bond strength of the normal opening at the steel concrete interface is also taken into account.

In Fig. 54 the corresponding deformed mesh obtained at the end of the test is presented. In this Figure, an exaggerated deformation of the stirrups at the bottom is found, since perfect bond is assumed between the stirrups and the concrete, which might seem unrealistic in this extreme case.

In both cases, it is found that a high level of corrosion introduced at the anchorage can lead to severe loss of strength and premature failure of the beam. In fact, in the tests without anchorage, bond between steel and concrete is lost before yielding of the steel reinforcement is reached. As a consequence, instead of the usual plateau corresponding to yielding of the steel, a softening branch is obtained in the load-displacement curve.

The stirrup confinement is observed at the upper steel-concrete interface: the detachment between steel and concrete close to midspan present on in Fig. 53 vanishes in Fig. 54. However, in the latter Figure, detachment of the cover is obtained at $x \approx 500$ mm and at midspan, when modelling spalling with splitting forces.

4 Experimental validation

Experimental results for corrosion are obtained with specimens which are submitted to chemical accelerated corrosion. Thus, the transition between non-corroded stage and corroded stage can not be experimentally validated. Instead, two simulations are performed:

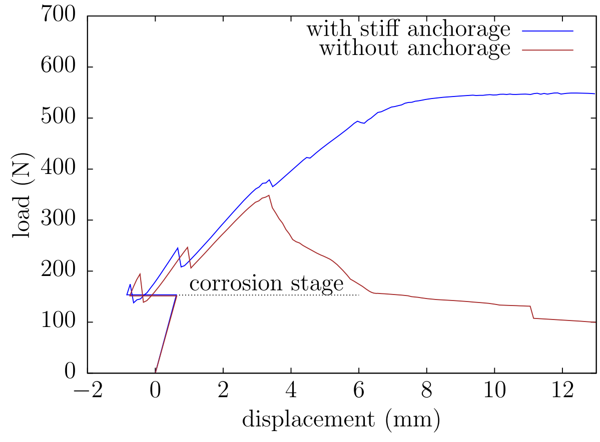

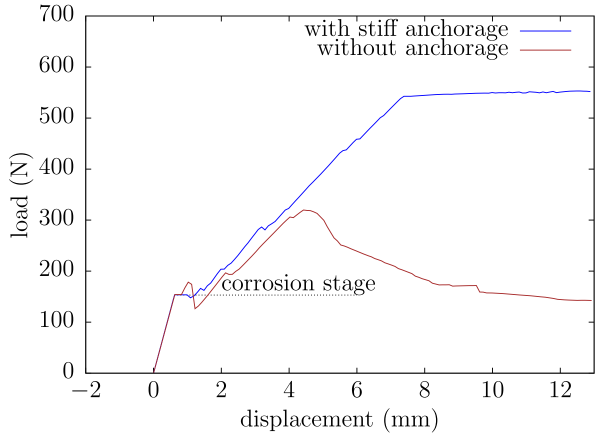

Fig. 52 Load-displacement curves with corrosion along the whole length of the beam (case 1, $F_1 = 153$ N), (a) without stirrups, spalling with volume expansion, (b) with stirrups, spalling with splitting forces

Fig. 53 Deformed mesh obtained at the end of the test corresponding to Fig. 52a, with severely corroded anchorage (case 1, $F_1 = 153$ N, displacement amplification factor 10)

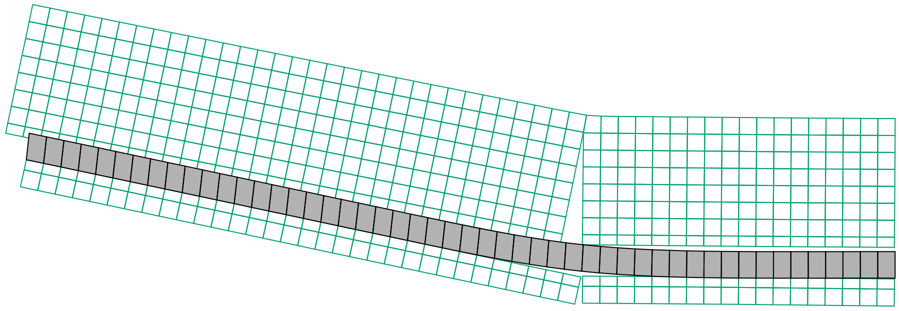

Fig. 54 Deformed mesh obtained at the end of the test corresponding to Fig. 52b, with severely corroded anchorage (case 1, $F_1 = 153$ N, displacement amplification factor 10)

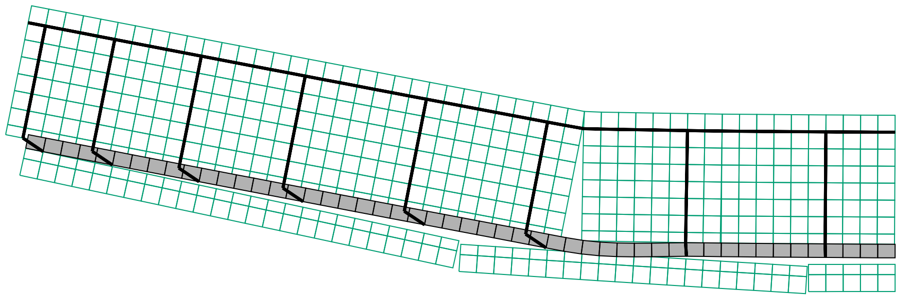

1. a non-corroded beam;
2. a corroded beam.

The experimental data and material characterization are taken from the works presented in Rodriguez et al. (1997); Sæter and Sand (2012); Nguyen et al. (2020). In the concrete used in case 2., calcium chloride (3% by weight of cement) was added to the mixing water to accelerate corrosion and a constant current density of $100\mu A/cm^2$ was applied to the reinforcement during 100 to 200 days.

The beams are simply supported, submitted to a four point bending test. An elastic-perfectly plastic behaviour is adopted for concrete. The concrete properties for both the non-corroded and corroded beams (beam D111 and beam D115, respectively, in Rodriguez et al. (1997); Sæter and Sand (2012)) are:

The beams are reinforced with 2 bars of 10 mm ($2\phi10$), with compressive reinforcement ($2\phi8$) and stirrups (sti $\phi6//0.17$ m). A bilinear relationship is

Beam	Young's modulus	character. strength	tensile strength	fracture energy
D111	$E_c = 32.2$ GPa	$f_{ck} = 50$ MPa	$f_t = 3.5$ MPa	$G_F =$ 0.116 N/mm
D115	$E_c = 28.3$ GPa	$f_{ck} = 31.4$ MPa	$f_t = 2.8$ MPa	$G_F =$ 0.091 N/mm

adopted for steel as shown in Fig.55a . The corresponding adopted properties are:

ϕ	Young's modulus E_s	yield stress f_{sy}	ultimate strength f_{su}
10	206 GPa	575 MPa	675 MPa
8	206 GPa	615 MPa	673 MPa
6	206 GPa	626 MPa	760 MPa

In Fig.56 the beam dimensions and reinforcement are presented, as well as the adopted mesh for half of the specimen due to symmetry. The resultant force is applied at $x = 950$ mm (see Fig.56). The location of the prescribed discontinuities is taken from Sæter and Sand (2012).

The pre-corrosion and post-corrosion bond-slip laws are given in Fig.55b and in appendix F. These relationships are multilinear approximations of the laws adopted in Sæter and Sand (2012).

In the experimental work obtained with beam D115, the measured level of corrosion for the tensile reinforcement was $\eta = 13.9\%$ (Rodriguez et al. 1997; Sæter and Sand 2012).

All effects due to corrosion are considered, except spalling which is introduced in the model at the transition or corrosion stage. Since it is found that spalling does not alter the ultimate load, the comparison between the simulation and experimental result remains conclusive.

In Fig.57a , the load-displacement curve obtained from the non-corroded test is compared to the experimental load-displacement result (beam D111). Both displacement control and load control are adopted, with the latter presented with a dashed line. A good agreement is found between numerical and experimental results.

In Fig.57b , the load-displacement curve obtained from the corroded test, adopting $\eta = 13.9\%$, is compared to the experimental load-displacement result (beam D115). Similar to the numerical result obtained by Sæter and Sand (2012), the numerical maximum load lies above the experimental one.

As previously stated, the reduction of the cross section of the steel reinforcement is found to be the main cause for the structural strength decrease under bending. According to the work presented in Gonzalez et al. (1995); Sæter and Sand (2012), if localized pitting attack occurs, the core reduction may be considerably greater than the core reduction obtained under uniform corrosion of the cross section. This is why one more simulation of the corroded beam is performed with $\eta = 18\%$, which gives rise to a better approximation of the experimental result, as shown in Fig.58.

In Fig.59, the deformed mesh corresponding to Fig.57b , obtained at the maximum load, is presented. As also observed in the work presented in Sæter and Sand (2012), two major cracks develop next to the symmetry line.

5 Final remarks

In this work, modelling of reinforced concrete under corrosion is performed. The material model is based on the damage mechanics theory and fracture mechanics concepts. Novel aspects are introduced with respect the the damage model presented in Alfaiate and Sluys (2017); Alfaiate et al. (2023) and are detailed in part I.

Under corrosion, several phenomena are taken into account, namely the degradation of the bond-slip relationship between steel and concrete, the core reduction of the steel cross section and spalling of the concrete cover. The numerical solution is based on the total iterative approach presented in Alfaiate and Sluys (2023), in which the refinements introduced in the material model are taken into account and return mapping is added. Numerical tests of reinforced concrete beams under bending are presented. Particular attention is paid to the dependence on the traction state under mixed-mode fracture and mode-II fracture under compression, spalling of the concrete cover and stirrup confinement. As an alternative to the volume expansion of the main reinforcement due to spalling, a new method is presented to allow for the modelling of the cover splitting in 2D, in which the volume expansion is *transferred* to the steel concrete interface, where splitting forces

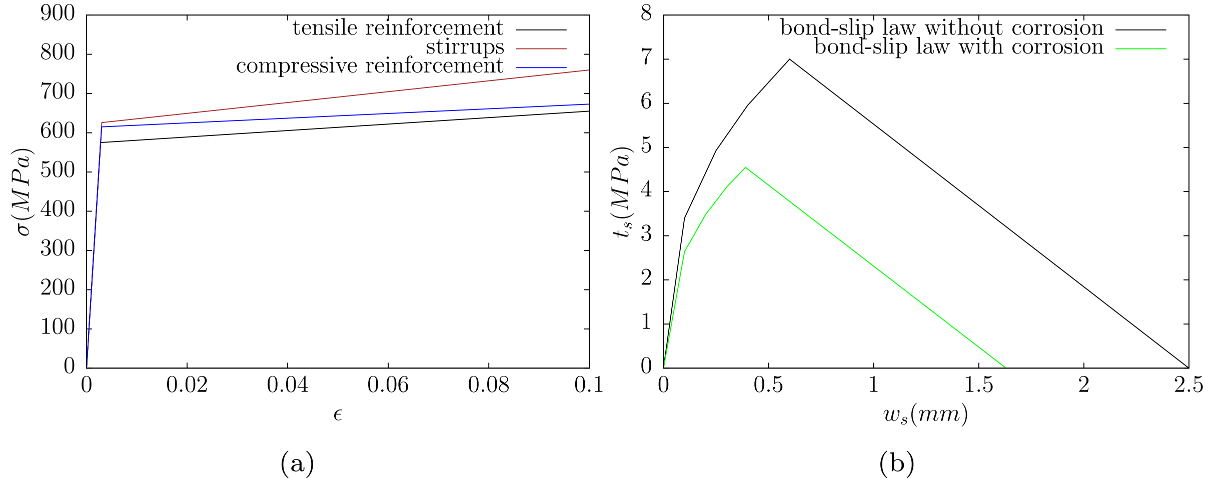

Fig. 55 (a) Bilinear relationship adopted for steel, (b) Bond-slip laws adopted without and with corrosion

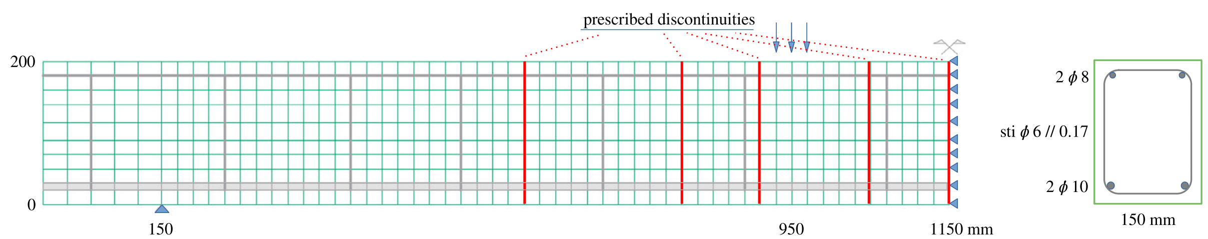

Fig. 56 Mesh (half of the specimen) and cross section of the beam

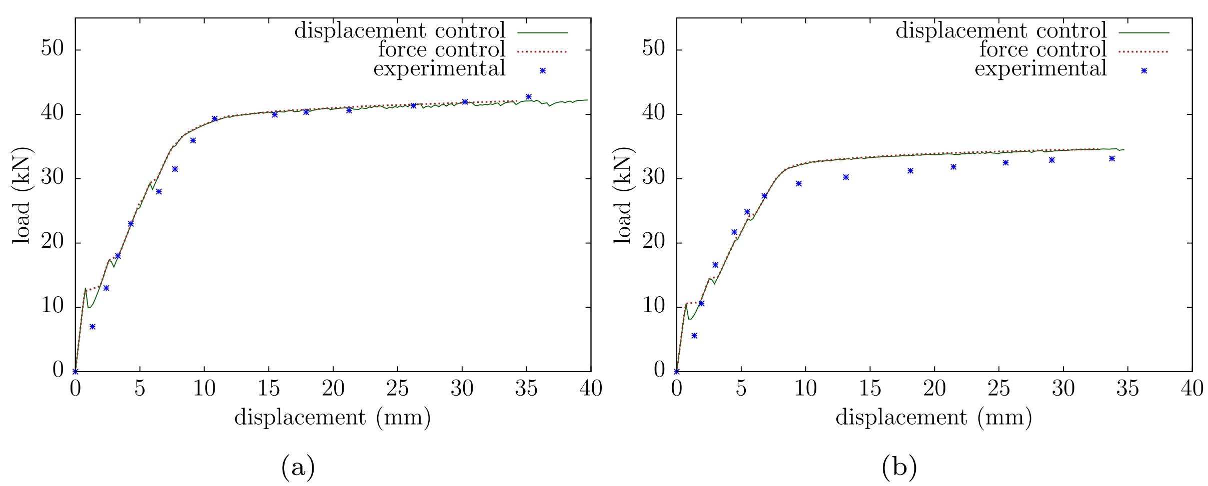

Fig. 57 (a) Experimental and numerical load-displacement results obtained without corrosion, (b) experimental and numerical load-displacement results obtained with corrosion, adopting $\eta = 13.9\%$

are introduced. A corrosion level of 20% is introduced, according to experimental evidence.

The main conclusions regarding corrosion are:

i. *degradation of the bond-slip relationship due to corrosion* leads to a decrease of the structure stiffness, but not to a decrease of the ultimate load;

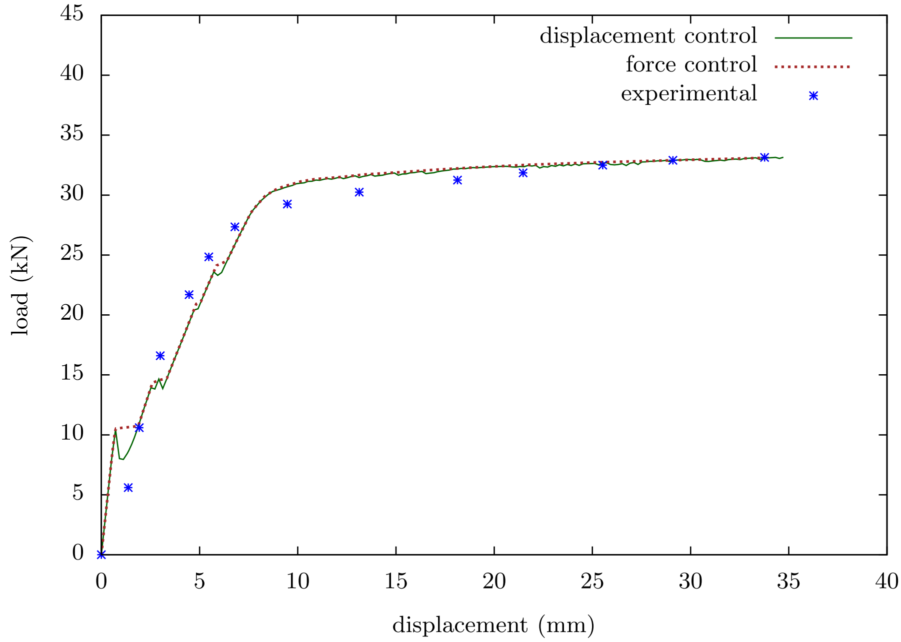

Fig. 58 Experimental and numerical load-displacement results obtained with corrosion, adopting $\eta = 18\%$

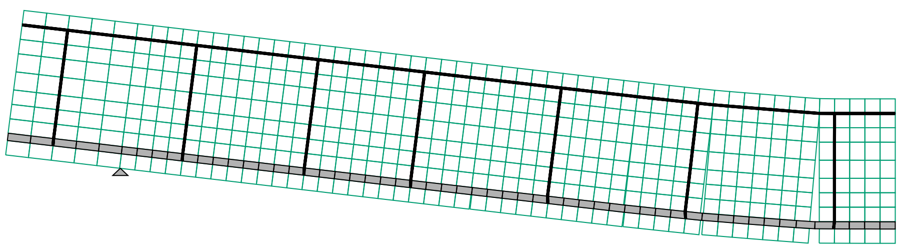

Fig. 59 Deformed mesh corresponding to Fig.57b (amplification displacement factor = 3)

ii. *the reduction of the cross section of the steel reinforcement* is the main cause for the decrease of the ultimate load which occurs approximately in the same proportion; this is an important result for design purposes;

iii. *mixed-mode fracture at the steel-concrete interface* leads to a decrease of the structure stiffness, accelerating the bond-slip degradation found in i.;

iv. *considering spalling by means of volume expansion of the main reinforcement*,

   (a) the effect of spalling of the concrete cover is found to be more important if corrosion is introduced only in the central zone of the beam. If corrosion affects the whole length of the beam, it seems that the volume expansion occurs without any important restraint introduced either by the structure or the boundary conditions, such that the stress state is not significantly altered;

   (b) stirrup confinement gives rise to significant differences at local level, namely concentrated stresses at the stirrup location, above and underneath the reinforcement. High compressive stresses are found above the reinforcement due to the confinement, whereas the tensile strength is reached below the reinforcement, leading to the local loss of adhesion between steel and concrete;

   (c) a strong fracture localization is found when corrosion is applied to the central zone of the beam, which leads to a significant stiffness decay and increase of displacement at the corrosion stage;

v. *considering spalling localised at the steel concrete interface by means of splitting forces*,

   (a) conversely to the previous case, the detachment of the concrete cover is clearly observed along the steel concrete interface;

(b) taking into account dependence of the bond strength on the normal opening of the interface, a more pronounced and widely distributed split of the steel concrete interface is found, both above and below the reinforcement;
(c) stirrup confinement prevents detachment of the concrete above the reinforcement, although it remains underneath the bar;
(d) stirrup confinement gives rise to higher, nonlinear compressive stresses at the top of the beam, leading to a smoother transition to the ultimate load in the load displacement curve;
(e) no fracture localization is found at the transition zone when corrosion is introduced at the central zone of the beam;
(f) as a consequence of the previous item, no stiffness decay is observed when corrosion is applied to the central zone of the beam, in which case a decrease of the displacement at the corrosion stage is observed;
(g) from items v.(a) to v.(f), it can be concluded that considering spalling by means of interface expansion gives rise to more realistic results in 2D than considering spalling by means of volume expansion;

vi. *slippage of the anchorage zone* was analyzed. It is found that, even by disregarding the standard bend or hook of the bars at the edge of the beam, severe slippage of the reinforcement only occurs if the damage due to corrosion further increases. In this case, a strong decay of the strength of the beam is found, leading to sudden premature failure. This effect is observed when spalling is modelled either with volume expansion of the reinforcement or splitting forces at the steel concrete interface.
vii. Experimental results obtained for a non-corroded beam and a corroded beam were compared to the numerical results obtained with the present model. A good approximation of the experimental results was obtained, emphasizing the importance of the core reduction due to corrosion.

Similar to the works presented in Alfaiate and Sluys (2023); Alfaiate et al. (2023), it was found that the Total Iterative Approach has proved to be a reliable numerical tool for the analysis of reinforced concrete with corrosion. Convergence was obtained in all examples, in which both the consistency condition and the constitutive relationships were obeyed. As a consequence, the obtained results can be regarded as reliable and trustworthy.

Finally, the adopted numerical and material model has the potential of providing a better understanding of the complex behaviour of reinforced concrete under corrosion. Moreover, the introduced strategy to model spalling with splitting forces, allows for the analyses of large structures in two dimensions, with considerable mesh and analysis simplification when compared to the simulations in 3D.

On the other hand, a more realistic description of the i) degradation of the steel-concrete bond-slip relation, ii) spalling of the concrete cover, iii) local radial cracking around the bar, iv) structural bending or shear cracking, v) compressive behaviour and vi) stirrup confinement, can only be achieved with a three-dimensional simulation. That should also be the aim of future research in this field. For this purpose, robust numerical methods must be adopted, such as the total iterative approach used in this work.

Author contributions 1 and 2 wrote the main maunscript. All authors reviewed the manuscript.

Funding The authors declare that they did not receive any grants or other forms of financial support for this research.

Data Availability Statement No datasets were generated or analysed during the current study.

Declarations

Competing interests The authors declare no competing interests.

A Summary of the material and numerical model

Table 2 Summary of the main aspects of the model: fracture mode, traction on the initial limit surface, energy dissipation, damage driving mechanism and return mapping

A. FRACTURE MODE:

1. MODE-I fracture: pure mode-I fracture, keeping the initial tensile strength f_{t0} and fracture energy G_F unchanged. Dependence on the shear traction is neglected;
2. MODE-II fracture: pure mode-II fracture, keeping the initial cohesion c_0 and fracture energy G_F^{II} unchanged. Dependence on the normal traction is neglected ;
3. MODE-II fracture under compression ($t_n \leq 0$): dependence on the limit surface is taken into account;
4. MIXED-MODE fracture ($t_n \geq 0$): dependence on the limit surface is taken into account.

B. TRACTION ON LIMIT SURFACE $\mathbf{t}^*$:

t1. traction $\mathbf{t}^*$ is defined on constant t_n load path

t2. traction $\mathbf{t}^*$ is defined on constant t_s load path;

t3. traction $\mathbf{t}^*$ is defined according to radial return mapping;

t4. traction $\mathbf{t}^*$ is defined according to no prescribed return mapping;

C. ENERGY DISSIPATION:

e1. linear variation of fracture energy:

$$G_F{}^* = G_F\left(t_n^*/f_{t0}\right), \quad G_F^{II*} = G_F^{II}\left(t_s^*/c_0\right); \qquad (6)$$

e2. quadratic variation of fracture energy:

$$G_F{}^* = G_F\left(t_n^*/f_{t0}\right)^2, \quad G_F^{II*} = G_F^{II}\left(t_s^*/c_0\right)^2. \qquad (7)$$

D. DAMAGE DRIVING MECHANISM:

i. mode-I - damage evolution is defined according to the modified fracture energy value G_F^* and the corresponding normal relationship;

ii. mode-II - damage evolution is defined according to the modified mode-II fracture energy value G_F^{II*} and the corresponding shear relationship;

iii. general mixed-mode - both fracture energies are modified to G_F^* and G_F^{II*}, and the final tractions are obtained with the linear or sigmoid weight functions;

iv.item:ddc damage driving mechanism under corrosion - damage (and stiffness) is evaluated from the transition mode between evolving corrosion states.

E. RETURN MAPPING:

a. radial - both normal and shear tractions are decreased proportionally, leading to isotropic damage evolution.

b. constant t_n - return mapping is performed keeping the normal traction constant;

c. constant t_s - return mapping is performed keeping the shear traction constant;

d. no prescribed return mapping .

Table 3 Possible combinations of fracture mode, traction on the initial limit surface, energy dissipation, damage driving mechanism and return mapping. Three groups defined according to the priority criterion marked in red: fracture mode, damage driving mechanism and return mapping.

LINE	FRACTURE MODE	TRACTION $\mathbf{t}^*$	ENERGY DISSIPATION	DAMAGE DRIVING MECHANISM	RETURN MAPPING
1	**1**	-	-	i	-
2	**2**	-	-	ii, iv	-
3	**3**	t1, t3, t4	e1, e2	ii, iv	a, b, d
4	**4**	t1, t2, t3, t4	e1, e2	i, ii, iii, iv	a, b, c, d
5	1, 4	t2	e1, e2	**i**	a, c, d
6	2, 3, 4	t1	e1, e2	**ii**	a, b, d
7	4	t3	e1, e2	**iii**	a
8	2, 3, 4	t1, t3, t4	e1, e2	**iv**	a, b, d
9	3, 4	t3	e1, e2	i, ii, iii, iv	**a**
10	3, 4	t1	e1, e2	ii	**b**
11	4	t2	e1, e2	i	**c**
12	1, 2	t4	e1, e2	i, ii, iv	**d**

B Adopted criteria in the numerical tests

Table 4 Fracture mode, damage driving mechanism and return mapping adopted in the numerical tests.

1. CRACK EVOLUTION:
 (a) mode-I fracture under mode-I damage driving mechanism (line 5 in Table 3),
. with no prescribed return mapping (line 12 in Table 3);
2. STEEL-CONCRETE INTERFACE:
 (a) mode-II fracture under mode-II damage driving mechanism (line 6 in Table 3),
 i) with no prescribed return mapping (line 12 in Table 3);
 (b) mode-II fracture under compression under mode-II damage driving mechanism (line 6 in Table 3),
 i) with constant t_n return mapping (line 10 in Table 3);
 ii) with no prescribed return mapping (line 12 in Table 3);
(c) mixed-mode fracture under mixed-mode damage driving mechanism (line 7 in Table 3),
 i) with radial return mapping (line 9 in Table 3);
3. CORROSION:
 (a) mode-II fracture under corrosion damage driving mechanism (line 8 in Table 3)
 (b) with radial return mapping (line 9 in Table 3)
 (c) with no prescribed return mapping (line 12 in Table 3).

C Estimation of the beam bending and shear resistance

According to Eurocode 2 (CEN 2004), the minimum reinforcement is given by

$$A_{s,min} = 0.26\frac{f_{ctm}}{f_{yk}} \cdot b \cdot d \approx 1 \text{ cm}^2 < A_s = 6.03 \text{ cm}^2 (3\phi 16), \quad (8)$$

where b is the width ($b = 30$ cm) and d is the effective height, $d = 16$ cm. The design bending resistance can be evaluated as:

$$M_{Rd} = z \cdot F_s, \quad (9)$$

where, the lever arm z is taken as $z \approx 0.9d$, and F_s is the maximum force acting at the reinforcement,

$$F_s = A_s \cdot f_{yd} = 6.03 \text{ cm}^2 \times 34.8 \text{ kN/cm}^2 = 210 \text{ kN}. \quad (10)$$

We get, $M_{Rd} = 0.9 \times 0.16 \times 210 = 30.2$ kN.m. The distributed load corresponding to $M_{Rd} = 30.2$ kN.m is $p_{Rd} = 60.4$ kN/m.

In the tests performed in the following, the expected ultimate bending moment, not taking corrosion into account, is given by

$$M_u = 0.9d \cdot A_s \cdot f_{yk} = 0.9 \times 0.16 \text{ m} \times 6.03 \text{ cm}^2 \times 40.0 \text{ kN/cm}^2 = 34.7 \text{ kN.m}, \quad (11)$$

with the corresponding ultimate distributed load $p_u \approx 70$ kN/m.

In Section 3.5 and according to Eurocode 2 (CEN 2004), the design shear resistance due to the stirrups can be evaluated as:

$$V_{Rd} = \frac{A_{sw}}{s} z \cdot \cot\theta \cdot f_{yd} \approx 136.3 \text{ kN}, \quad (12)$$

where $A_{sw} = 1.57$ cm^2 is the area of the stirrups ($2\phi 10$), minimum spacing is $s \approx 0.1$ m near the support, $z \approx 0.9d = 0.9 \times 0.16$ m, where d is the effective depth, z is the lever arm, θ is the angle of the inclined struts in the shear truss, taken as $\theta = 30°$ and $f_{yd} = 348$ MPa.

Since, from (11), it is found that $p_u \approx 70$ kN/m, the applied load gives rise to a maximum reaction force of $R \approx 70$ kN. The corresponding maximum shear force is

$$V_{su} = R - z \cdot \cot\theta \times 70 \text{ kN/m} \approx 52.5 \text{ kN}, \quad (13)$$

such that the design shear force $V_{sd} < 52.5 \text{ kN} \ll V_{Rd}$.

D Bond-slip laws adopted with and without corrosion

Table 5 Initial and final multilinear mode-II fracture relationships adopted for bond-slip.

Initial bond-slip law ($\eta = 0$) w_s (mm)	t_s (MPa)	Final bond-slip law ($\eta_f = 0.2$) w_s (mm)	t_s (MPa)
0.20	6.371	0.20	3.159
0.617	8.749	0.42	3.565
1.5	7.397	1.5	2.816
2.0	6.547	2.0	2.491
2.5	5.791	2.5	2.203
5.0	3.136	5.0	1.193
15.0	0.270	15.0	0.103
30.0	0.000	30.0	0.000

E Definition of the weighted value c_w for the crack opening across the width of the beam

As stated in part I, parameter c_w accounts for the variation of the crack opening across the width (see also Fig.23 in part I). In equation (45) of part I, c_w is defined as a function of the relation between the number of bars × the diameter of the bars and the width of the beam. As a consequence, c_w increases with the percentage of reinforcement $\rho = A_s/bd$; for instance, if the maximum percentage $\rho = 4\%$ according to CEN (2004) is attained, the value of c_w should be taken close to 1. On the other hand, a minimum value for $c_w \approx 0.5$ is suggested for minimum reinforcement. In fact, c_w can be understood as a weighted function defining the average crack opening across the width. The adopted beam is moderately reinforced ($\rho = 1.2\%$), with large internal spacing between the bars (circa 90 mm). This is why the weighted crack opening is reduced from $w_n^{spalling} = 1.53$ mm to a "round" value of $w_n^{eq} = 1$ mm, leading to $c_w = 0.65$. Thus, this approximation is essentially a strategy which translates 3D information regarding the cracking distribution across the width into a 2D formulation.

F Bond-slip laws adopted in the experimental validation

Table 6

Table 6 Multilinear bond-slip laws corresponding to Fig.55b .

specimen without corrosion		specimen with corrosion	
w_s (mm)	t_s (MPa)	w_s (mm)	t_s (MPa)
0.10	3.40	0.10	2.64
0.25	4.93	0.20	3.48
0.40	5.95	0.30	4.10
0.60	7.00	0.39	4.55
2.50	0.00	1.63	0.00

References

Alfaiate J, Sluys LJ (2017) On the modelling of mixed-mode discrete fracture: Part ii - inclusion of dilatancy. Eng Fract Mech 182:245–264

Alfaiate J, Sluys LJ (2023) A novel, total-iterative approach to model quasi-brittle materials. Eng Fract Mech 277. https://doi.org/10.1016/j.engfracmech.2022.108955

Alfaiate J, Sluys LJ, Costa A (2023) Modelling fracture due to corrosion and mechanical loading in reinforced concrete. Int J Fract 243:143–168. https://doi.org/10.1007/s10704-023-00733-8

CEN (2004) En 1992-1-1: Eurocode 2: Design of concrete structures - part 1-1: General rules and rules for buildings

Dias-da-Costa D, Alfaiate J, Júlio E (2007) A comparative study on the numerical modelling of discrete fracture in quasi-brittle materials using strong discontinuities. In: Yagawa G (ed) Proceedings of the Third Asian-Pacific Congress on Computational Mechanics (APCOM 07) in conjunction with Eleventh International Conference on Enhancement and Promotion of Computational Methods in Engineering and Science (EPMESC XI), Kyoto, Japan, p 572

Dias-da-Costa D, Alfaiate J, Sluys L, Júlio E (2010) A comparative study on the modelling of discontinuous fracture by means of enriched nodal and element techniques and interface elements. Int J Fract 161(1):97–119

Fang C, Lundgren K, Chen L, Zhu C (2004) Corrosion influence on bond in reinforced concrete. Cem Concr Res 34:2159–2167

Fang C, Lundgren K, Plos M, Gyltoft K (2006) Bond behaviour of corroded reinforcing steel bars in concrete. Cem Concr Res 36:1931–1938

Gonzalez JA, Andrade C, Alonso C, Feliu S (1995) Comparison of rates of general corrosion and maximum pitting penetration on concrete embedded steel reinforcement. Cem Concr Res 25(2):257–264

Guzmán S, Gálvez JC (2017) Modelling of concrete cover cracking due to non-uniform corrosion of reinforcing steel. Constr Build Mater 155:1063–1071

Guzmán S, Gálvez JC, Sancho JM (2011) Cover cracking of reinforced concrete due to rebar corrosion induced by chloride penetration. Cem Concr Res 41:893–902

Guzmán S, Gálvez JC, Sancho JM (2012) Modelling of corrosion-induced cover cracking in reinforced concrete by an embedded cohesive crack finite element. Eng Fract Mech 93:92–107

Guzmán S, Gálvez JC, Sancho JM (2014) Modelling of chloride ingress into concrete through a single-ion approach. application to an idealized surface crack pattern. Int J Numer Anal Meth Geomech 38:1683–1706

Hillerborg A, Modeer M, Petersson PE (1976) Analysis of crack formation and crack growth in concrete by means of fracture mechanics and finite elements. Cem Concr Res 6(6):773–782

Jiang C, Wu YF, Dai MJ (2018) Degradation of steel-to-concrete bond due to corrosion. Constr Build Mater 158:1073–1080

Kikuchi N, Oden JT (1988) Contact problems in elasticity: a study of variational inequalities and finite element methods. SIAM Studies in Applied Mathematics 8, Philadelphia

Lin H, Zhao X, Sun M (2014) Effects of stirrups on bond behaviour between concrete and corroded steel bars. In: Olex J, Weiss WJ (eds) Proceedings of the 4th International Conference on the Durability of Concrete Structures, Purdue University Press, West Lafayette, Indiana, USA, pp 122–126

Nguyen TH, Nghiem MH, Nguyen DD (2020) Evaluation of loading capacity of corroded reinforced concrete beams using experiment and finite element method. Journal of Materials and Engineering Structures 7:510–517

Ožbolt J, Oršanić F, Balabanić G (2017) Modelling processes related to corrosion of reinforcement in concrete: coupled 3d finite element model. Structure and Infrasctruture Engineering 13:135–146

PBroomfield J, (1997) Corrosion of Steel in Concrete: Understanding Investigation on Repair. E & FNSPON, USA

Rodriguez J, Ortega ML, Casal J (1997) Load carrying capacity of concrete structures with corroded reinforcement. Constr Build Mater 11(4):239–248

Sæter I, Sand B (2012) Fem simulations of reinforced concrete beams attacked by corrosion. ACI Struct J 39(2):15–31

Sanz B, Planas J, Sancho JM (2013) An experimental and numerical study of the pattern of cracking of concrete due to steel reinforcement corrosion. Eng Fract Mech 114:26–41

Sanz B, Planas J, Sancho JM (2015) A closer look to the mechanical behaviour of the oxide layer in concrete reinforcement corrosion. Int J Solids Struct 62:256–268

Sanz B, Planas J, Sancho JM (2016) Study of the influence of the oxide and concrete parameters on the results of accelerated corrosion tests. Procedia Structural Integrity 2:2849–2856

Sanz B, Planas J, Sancho JM (2017) A method to determine the constitutive parameters of oxide in accelerated corrosion tests of reinforced conrete specimens. Cem Concr Res 101:68–81

Silva J (2018) Análise do comportamento de vigas de betão armado com dano induzido por deterioração. Master's thesis, Instituto Superior Técnico, Universidade de Lisboa, Portugal

Wu Y, Zhao X (2013) Unified bond stress-slip model for reinforced concrete. ASCE Journal of Structural Engineering 139(11):1951–1962. https://doi.org/10.1061/(ASCE)ST.1943-541X.0000747